

CEERS Key Paper IV: Galaxies at $4 < z < 9$ are Bluer than They Appear — Characterizing Galaxy Stellar Populations from Rest-Frame ~ 1 micron Imaging

CASEY PAPOVICH,^{1,2} JUSTIN W. COLE,^{1,2} GUANG YANG,^{3,4} STEVEN L. FINKELSTEIN,⁵ GUILLERMO BARRO,⁶ VÉRONIQUE BUAT,⁷
DENIS BURGARELLA,⁷ PABLO G. PÉREZ-GONZÁLEZ,⁸ PAOLA SANTINI,⁹ LISE-MARIE SEILLÉ,⁷ LU SHEN,^{1,2}
PABLO ARRABAL HARO,¹⁰ MICAELA B. BAGLEY,⁵ ERIC F. BELL,¹¹ LAURA BISIGELLO,^{12,13} ANTONELLO CALABRÒ,⁹
CAITLIN M. CASEY,⁵ MARCO CASTELLANO,⁹ KATHERINE CHWOROWSKY,^{5,*} NIKKO J. CLERI,^{1,2} M. C. COOPER,¹⁴
LUCA COSTANTIN,⁸ MARK DICKINSON,¹⁰ HENRY C. FERGUSON,¹⁵ ADRIANO FONTANA,⁹ MAURO GIAVALISCO,¹⁶
ANDREA GRAZIAN,¹³ NORMAN A. GROGIN,¹⁵ NIMISH P. HATHI,¹⁵ BENNE W. HOLWERDA,¹⁷ TAYLOR A. HUTCHISON,^{18,†}
JEYHAN S. KARTALTEPE,¹⁹ LISA J. KEWLEY,²⁰ ALLISON KIRKPATRICK,²¹ DALE D. KOCEVSKI,²² ANTON M. KOEKEMOER,¹⁵
REBECCA L. LARSON,^{5,*} ARIANNA S. LONG,^{5,*} RAY A. LUCAS,¹⁵ LAURA PENTERICCI,⁹ NOR PIRZKAL,^{23,15}
SWARA RAVINDRANATH,¹⁵ RACHEL S. SOMERVILLE,²⁴ JONATHAN R. TRUMP,²⁵ STEPHANIE M. URBANO STAWINSKI,¹⁴
BENJAMIN J. WEINER,²⁶ STEPHEN M. WILKINS,^{27,28} L. Y. AARON YUNG,^{18,†} AND JORGE A. ZAVALA²⁹

¹Department of Physics and Astronomy, Texas A&M University, College Station, TX, 77843-4242 USA

²George P. and Cynthia Woods Mitchell Institute for Fundamental Physics and Astronomy, Texas A&M University, College Station, TX, 77843-4242 USA

³Kapteyn Astronomical Institute, University of Groningen, P.O. Box 800, 9700 AV Groningen, The Netherlands

⁴SRON Netherlands Institute for Space Research, Postbus 800, 9700 AV Groningen, The Netherlands

⁵Department of Astronomy, The University of Texas at Austin, Austin, TX, USA

⁶Department of Physics, University of the Pacific, Stockton, CA 90340 USA

⁷Aix Marseille Univ, CNRS, CNES, LAM Marseille, France

⁸Centro de Astrobiología (CAB), CSIC-INTA, Ctra. de Ajalvir km 4, Torrejón de Ardoz, E-28850, Madrid, Spain

⁹INAF - Osservatorio Astronomico di Roma, via di Frascati 33, 00078 Monte Porzio Catone, Italy

¹⁰NSF's National Optical-Infrared Astronomy Research Laboratory, 950 N. Cherry Ave., Tucson, AZ 85719, USA

¹¹Department of Astronomy, University of Michigan, 1085 S. University Ave, Ann Arbor, MI 48109-1107, USA

¹²Dipartimento di Fisica e Astronomia "G. Galilei", Università di Padova, Via Marzolo 8, I-35131 Padova, Italy

¹³INAF-Osservatorio Astronomico di Padova, Vicolo dell'Osservatorio 5, I-35122, Padova, Italy

¹⁴Department of Physics & Astronomy, University of California, Irvine, 4129 Reines Hall, Irvine, CA 92697, USA

¹⁵Space Telescope Science Institute, 3700 San Martin Dr., Baltimore, MD 21218, USA

¹⁶University of Massachusetts Amherst, 710 North Pleasant Street, Amherst, MA 01003-9305, USA

¹⁷Physics & Astronomy Department, University of Louisville, 40292 KY, Louisville, USA

¹⁸Astrophysics Science Division, NASA Goddard Space Flight Center, 8800 Greenbelt Rd, Greenbelt, MD 20771, USA

¹⁹Laboratory for Multiwavelength Astrophysics, School of Physics and Astronomy, Rochester Institute of Technology, 84 Lomb Memorial Drive, Rochester, NY 14623, USA

²⁰Center for Astrophysics | Harvard & Smithsonian, 60 Garden Street, Cambridge, MA 02138, USA

²¹Department of Physics and Astronomy, University of Kansas, Lawrence, KS 66045, USA

²²Department of Physics and Astronomy, Colby College, Waterville, ME 04901, USA

²³ESA/AURA Space Telescope Science Institute

²⁴Center for Computational Astrophysics, Flatiron Institute, 162 5th Avenue, New York, NY, 10010, USA

²⁵Department of Physics, 196 Auditorium Road, Unit 3046, University of Connecticut, Storrs, CT 06269, USA

²⁶MMT/Steward Observatory, University of Arizona, 933 N. Cherry Ave., Tucson, AZ 85721, USA

²⁷Astronomy Centre, University of Sussex, Falmer, Brighton BN1 9QH, UK

²⁸Institute of Space Sciences and Astronomy, University of Malta, Msida MSD 2080, Malta

²⁹National Astronomical Observatory of Japan, 2-21-1 Osawa, Mitaka, Tokyo 181-8588, Japan

ABSTRACT

We present results from the *Cosmic Evolution Early Release Survey* (CEERS) on the stellar-population parameters for 28 galaxies with redshifts $4 < z < 9$ using imaging data from the *James Webb Space Telescope* (JWST) Mid-Infrared Instrument (MIRI) combined with data from the *Hubble Space Telescope* and the *Spitzer Space Telescope*. The JWST/MIRI 5.6 and 7.7 μm data extend the coverage of the rest-frame spectral-energy

Corresponding author: Casey Papovich

papovich@tamu.edu

distribution (SED) to nearly 1 micron for galaxies in this redshift range. By modeling the galaxies’ SEDs the MIRI data show that the galaxies have, on average, rest-frame UV (1600 Å) – *I*-band colors 0.4 mag bluer than derived when using photometry that lacks MIRI. Therefore, the galaxies have lower (stellar)-mass-to-light ratios. The MIRI data reduce the stellar masses by $\langle \Delta \log M_* \rangle = 0.25$ dex at $4 < z < 6$ (a factor of 1.8) and 0.37 dex at $6 < z < 9$ (a factor of 2.3). This also reduces the star-formation rates (SFRs) by $\langle \Delta \log \text{SFR} \rangle = 0.14$ dex at $4 < z < 6$ and 0.27 dex at $6 < z < 9$. The MIRI data also improve constraints on the *allowable* stellar mass formed in early star-formation. We model this using a star-formation history that includes both a ‘burst’ at $z_f = 100$ and a slowly varying (“delayed- τ ”) model. The MIRI data reduce the allowable stellar mass by 0.6 dex at $4 < z < 6$ and by ≈ 1 dex at $6 < z < 9$. Applying these results globally, this reduces the cosmic stellar-mass density by an order of magnitude in the early universe ($z \approx 9$). Therefore, observations of rest-frame $\gtrsim 1 \mu\text{m}$ are paramount for constraining the stellar-mass build-up in galaxies at very high-redshifts.

1. INTRODUCTION

There is growing evidence that galaxies must have started forming stars very quickly following the Big Bang. Theory predicts the first stars should form at $z \gtrsim 20$ (e.g., Barkana & Loeb 2001; Miralda-Escudé 2003; Yoshida et al. 2003; Wise et al. 2012; Visbal et al. 2020). The ionization from these sources is needed to explain observations that the hydrogen-neutral fraction of the intergalactic medium (IGM) was 50% by $z \sim 8$ (Planck Collaboration et al. 2020),¹ and to account for the absorption profile of the 21 cm signal at $z \sim 20$ (e.g., Bowman et al. 2018). Indeed, early observations from *JWST* have already identified candidates for galaxies at $z \gtrsim 15$ (Curtis-Lake et al. 2022; Donnan et al. 2022; Finkelstein et al. 2022a; Robertson et al. 2022). Spectroscopy from *JWST* of galaxies at $z \sim 8-9$ shows emission lines from heavy elements that appear to require metallicities of $\approx 5-10\% Z_\odot$ (Arellano-Córdova et al. 2022; Fujimoto et al. 2022; Heintz et al. 2022; Langeroodi et al. 2022; Matthee et al. 2022; Schaerer et al. 2022; Trump et al. 2022; Curti et al. 2023; Katz et al. 2023), implying these galaxies have experienced at least one (and probably multiple) generation(s) of previous stars. This is consistent with earlier detections of metal lines in $z > 6$ galaxies from ground-based telescopes (e.g., Stark et al. 2017; Hutchison et al. 2019). All of these results point to the fact that star formation began early and those early generations of stars enriched the universe with heavy elements.

It is then important to consider how we may constrain the history of star-formation in these early galaxies. The number of stars (and therefore the *stellar mass*) in galaxies appears to rise rapidly. The (co-moving) stellar mass density in galaxies at $z \sim 5-6$ (when the age of the Universe is ≈ 1 Gyr) is already 1% of the present value (e.g., Madau & Dickinson 2014; Finkelstein 2016), where simulations and theory require the stars in those objects formed at much earlier times. Even early *JWST* observations find some evidence for massive galaxies at $z > 7$ (Labbé et al. 2022) with some

candidate objects having masses, $\log M_*/M_\odot > 11$ (as large as the stellar mass of the Milky Way *today*, e.g., Papovich et al. 2015). Such objects would be in tension with galaxy formation models (Boylan-Kolchin 2022) where there are not sufficient numbers of massive dark-matter halos to support these objects, even if *all* the baryons in the halos are in the form of stellar mass. However, the uncertainty in these measurements is in the assumed star-formation histories, the contributions of emission lines to the photometric measurements from broad-band data (e.g., Endsley et al. 2022; Pérez-González et al. 2022; Steinhardt et al. 2022), and the effects young stellar populations “outshining” older stellar populations in the integrated emission of galaxies (e.g., Giménez-Arteaga et al. 2022). Clearly there are unknown systematics in the assumptions of the data analysis, or missing physics in our theoretical understanding of stellar populations and galaxy formation, or some combination of all of these things. It is therefore crucial to understand constraints on the stellar masses (which are the integral of the star-formation histories) as much as possible.

Motivated by these issues, in this *Paper* we use new data from *JWST* to better constrain the stellar masses, star-formation rates (SFRs), and star-formation *histories* of galaxies during the first one and a half billion years after the Big Bang ($z > 4$). One of the problems with initial studies from *JWST* is that they currently rely entirely on observations from *JWST*’s Near-IR Camera (NIRcam), which only probes to wavelengths $\lesssim 5 \mu\text{m}$, or about 6000 Å rest-frame for $z = 6-7$ galaxies. This complicates the ability to disentangle massive galaxies with older stellar populations from younger, dusty galaxies or galaxies with emission lines with extreme equivalent widths (see discussion in Antwi-Danso et al. 2022, and recent work by Giménez-Arteaga et al. 2022 who find evidence for older stellar populations mixed with recent bursts in spatially resolved studies using *JWST*/NIRCam data). To better constrain the SEDs of these galaxies requires observations at longer wavelengths. This is where *JWST*/MIRI is important as it has the sensitivity to detect $z \approx 10$ galaxies at rest-frame $1 \mu\text{m}$ (see Bisigello et al. 2017). Previous work on this subject has been limited to data from the *Spitzer Space Telescope*, which is primarily sensitive to the emission such distant galaxies at 3.6 to 8.0 μm . *JWST* offers immense gains to *Spitzer*: *JWST* has a collecting area that is 45 times larger than that of *Spitzer*, and the larger aperture provides

* NSF Graduate Fellow

† NASA Postdoctoral Fellow

‡ NASA Hubble Fellow

¹ The Planck Collaboration et al. (2020) analysis also suggests a non-zero optical depth of CMB photons scattering off free electrons at $z \approx 15$, which implies ionization of the IGM had begun by this epoch.

image quality (i.e., angular resolution) that is improved by a factor of order 10 (Rigby et al. 2022). These gains are especially manifest at longer wavelengths, and make *JWST* 5.6 and 7.7 μm data vastly more sensitive than *Spitzer*.

The outline for the *Paper* is as follows. In Section 2 we discuss the CEERS dataset and the ancillary datasets used in this study. We also discuss the processes to create (and validate) the flux densities of galaxies in the CEERS *JWST*/MIRI data at 5.6 and 7.7 μm . In Section 2.2 we discuss the sample of $4 < z < 9$ galaxies used in this study, and we present the MIRI data for these objects. In Section 3 we discuss the analysis methods to derive constraints on the galaxy stellar populations. In Section 4 we discuss the resulting improvements that including the MIRI data provide on constraints on the galaxies stellar populations (specifically their stellar-masses and SFRs) derived from fitting stellar population models to the observed photometry. In Section 4.4 we discuss constraints on the range of allowed stellar masses in these high redshift galaxies by allowing for an early (“maximally old”) burst of stars at $z = 100$, and we show that adding the MIRI data improves the limit on this hypothetical population of $z = 100$ stars by a factor of 6 to 10 for galaxies at $4 < z < 9$. In Section 5 we discuss the implications these constraints have for our understanding of galaxy colors, stellar populations at these high redshifts, and the evolution of the galaxy stellar mass density, in particular during the epoch of reionization, and what this could mean for future studies of galaxies at higher redshifts (from *JWST*). In Section 6 we present our conclusions and prospects for future studies.

Throughout we use a flat cosmology with $\Omega_{m,0} = 0.315$, $H_0 = 67.4 \text{ km s}^{-1} \text{ Mpc}^{-1}$ (Planck Collaboration et al. 2020). All magnitudes reported here are on the *Absolute Bolometric* (AB) system (Oke & Gunn 1983). Throughout we use Chabrier (2003) initial mass function (IMF) for all stellar masses and SFRs. We denote magnitudes measured in the MIRI F560W and F770W bands as [5.6] and [7.7], respectively. Similarly, we denote magnitudes measured in IRAC Channel 1 (3.6 μm), Channel 2 (4.5 μm), Channel 3 (5.8 μm), and Channel 4 (8.0 μm) as [3.6], [4.5], [5.8], and [8.0], respectively.

2. DATA AND SAMPLE

2.1. MIRI Catalog

We use the data release DR0.5 images produced by the CEERS team for the MIRI 3 and MIRI 6 fields (see Finkelstein et al. 2022a)². These data were acquired in 2022 June 21 and 22. The data properties and its reduction are discussed elsewhere (Yang et al. 2022 in prep), but we provide a summary here. The data were processed using the *JWST* Calibration Pipeline (v1.7.2) using the default parameters for stage 1 and 2. We then removed the backgrounds with a custom routine that combines images taken in the same bandpass but from different fields and/or dither positions (rejecting pix-

els in each image that contain galaxies) in order to create a “super-background” image. We then removed this background from each image and applied an astrometric correction to each image prior to processing them with stage 3 of the pipeline. This produced the final science images (extension `i2d`), rms images (extension `rms`, which account for Poisson, readout, and correlated pixel noise; see Yang et al. 2022 in prep), and weight maps (`wht`) for each field with a pixel scale of 0.09”, registered astrometrically to the existing *HST*/CANDELS v1.9 WFC3 and ACS images (see Koekoer et al. 2011; Bagley et al. 2022²).

For the purpose of this study we are interested in sources detected in the MIRI data, so we create a catalog of sources derived from these images. Prior to object detection we convolved the 5.6 μm image to match the image quality of the 7.7 μm image. For this step, we constructed an “effective” point source function (ePSF) for each image by identifying unblended stars using the `photutils` (v1.5.0) `detection` task, and modeling them with the `photutils` `psf` task. This produced model ePSFs with measured full-width at half maxima (FWHM) of 0.24” and 0.28”, for the F560W and F770W images, respectively. This is consistent with the expected image quality, but takes into account the exact dithering and reduction steps for the CEERS MIRI data. We then used `PyPHER` (Boucaud et al. 2016b) to construct a convolution kernel to match the image quality of the model ePSFs. We applied these kernels to each F560W image, creating a “PSF-matched” image. Our tests on point sources in the PSF-matched F560W and F770W images show that we measure the same fraction of light to better than 2% in fixed circular apertures of radii larger than 0.35”.

We then created a detection image constructed from the sum of the MIRI F560W and F770W science images (using the extension `sci`) weighted by the appropriate weight image (using the extension `wht`). We also created a detection weight-map as the sum of the weights for these images. We then created F560W and F770W catalogs using Source Extractor (SE, version 2.19.5; Bertin & Arnouts 1996) in “dual-image” mode using the detection image (and its weight map) for object detection, where we measured photometry in the PSF-matched F560W and F770W image. We used the parameters in Table 1. We then measured fluxes and magnitudes using circular apertures of 0.9” diameter, and we scaled these to a total aperture (`MAG_AUTO`) measured for each source in the detection image. Uncertainties for each object are measured from the rms image in the same apertures, and scaled to a total magnitude in the same way. Figure 1 shows the distribution of the MIRI sources with signal-to-noise (SNR) ≥ 3 in F560W or F770W (compared with our galaxy sample, discussed below in 2.2).

We compared the MIRI flux densities for sources F560W and F770W against those for bright objects from existing IRAC 5.8 and 8.0 μm catalogs Stefanon et al. (2017). For bright objects ($[5.8]$ or $[8.0] \leq 22$ AB mag) in the IRAC data, we measure small offsets of $\Delta m = [5.8] - [5.6] = 0.16$ mag between the IRAC 5.8 and MIRI 5.6 data, and $\Delta m = [8.0] -$

² <https://ceers.github.io/releases.html>

Table 1. CEERS MIRI F560W and F770W SExtractor Parameter Settings

SExtractor Parameter	Value
(1)	(2)
DETECT_MINAREA	10 pixels
DETECT_THRESH	1.3
ANALYSIS_THRESH	1.3
FILTER_NAME	gauss_2.5_5x5 ^a
WEIGHT_TYPE	MAP_WEIGHT,MAP_RMS
DEBLEND_NTHRESH	32
DEBLEND_MINCONT	0.005
MAG_ZEROPOINT	25.701 ^b
PIXEL_SCALE	0.09 arcsec
BACK_TYPE	AUTO
BACK_FILTERSIZE	5 pixels
BACK_SIZE	32 pixels
BACKPHOTO_THICK	8
BACKPHOTO_TYPE	LOCAL
SEEING_FWHM	0.3 arcsec

NOTE—SE was run using the weighted sum of the PSF-matched F560W and F770W images for detection, and using the images separately for photometry. All other SE parameters are set to the program defaults (for SExtractor v.2.19.5).

^aThis is a Gaussian kernel with $\sigma=2.5$ pixels and size 5×5 pixel² used to filter the image for source detection.

^bThe AB magnitude zeropoint for the images, converting from the *JWST* default of MJy sr⁻¹ to μ Jy pixel⁻¹ at the 0.09'' pixel⁻¹ scale.

[7.7] = 0.07 mag between the IRAC 8.0 and MIRI 7.7 data (i.e., the MIRI flux densities are slightly brighter). Most of these offsets can be explained by differences in the shape of the MIRI and IRAC passbands and because of differences in the angular resolution of the instruments (MIRI has a PSF FWHM smaller by a factor of more than seven). These tests are discussed more fully in Yang et al. (2022 in prep), but this gives us confidence that the MIRI data are calibrated to better than $\simeq 0.1 - 0.2$ mag.

2.2. Galaxy Sample

For this study we use galaxies identified in the CEERS/MIRI first epoch fields with redshifts $4.3 < z < 10$. The lower redshift bound is selected to ensure the *HST* photometric data (used for galaxy photometric redshifts) probes the redshifted Lyman-break. The upper redshift limit includes the highest redshift galaxies detectable by *HST*/WFC3

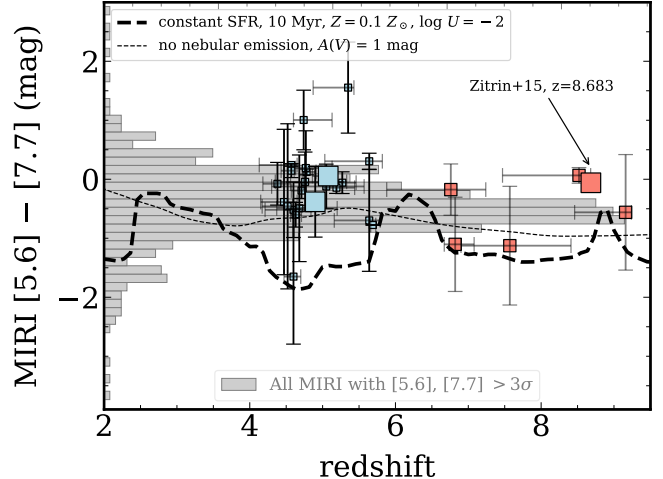


Figure 1. MIRI [5.6] – [7.7] colors of the sample studied here as a function of redshift. The data points (and error bars) denote the 28 objects studied here (blue-shaded points have $4 < z < 6$ and red-shaded points have $6 < z < 10$). The three sources with spectroscopic redshifts are indicated with larger symbols (the source $z = 8.683$ published by Zitrin et al. 2015 is labeled). The gray histogram shows the distribution of MIRI colors for all objects detected in both bands in CEERS. The bold-dashed line shows the expected color of a stellar population with nebular emission as discussed in the text.

data (Bouwens et al. 2019; Finkelstein et al. 2022b). This is illustrated in Figure 2 which shows that for galaxies around $z \sim 5$ and $z \sim 9$, the *HST*/ACS and WFC3 data constrain this break. This improves the quality of the sample (as compared to, for example, using galaxies at $z \approx 3$ where the Lyman-break shifts blueward of the *HST*/ACS F606W band).

The parent sample for our study is the catalog from Finkelstein et al. (2022b), which uses the existing *HST*/ACS, WFC3 and *Spitzer*/IRAC 3.6 and 4.5 μ m data to select photometric samples of galaxies at these high redshifts. The data include both the imaging from the original CANDELS survey (*HST*/ACS F606W, F814W, WFC3 F125W, F160W) and additional imaging from WFC3 F140W (see Footnote 2). Finkelstein et al. (2022b) then use these data to measure photometric redshifts and redshift probability distributions, $P(z)$ for each object.

We then matched objects from the catalog from Finkelstein et al. (2022b) with objects in our MIRI catalogs that are detected with $S/N > 3$ in either the MIRI 5.6 or 7.7 μ m data (Section 2.1) using a matching radius of 0.5''. This sample includes 29 objects, though one object was later identified as foreground star and removed. Table 5 which lists the observed properties of the 28 galaxies in the sample, their ID numbers from Finkelstein et al. (2022b), their *HST*/F160W flux densities the MIRI 5.6 and 7.7 μ m flux densities. The table includes the photometric redshifts derived by Finkelstein et al. (including the 16th and 84th-percentile range from the

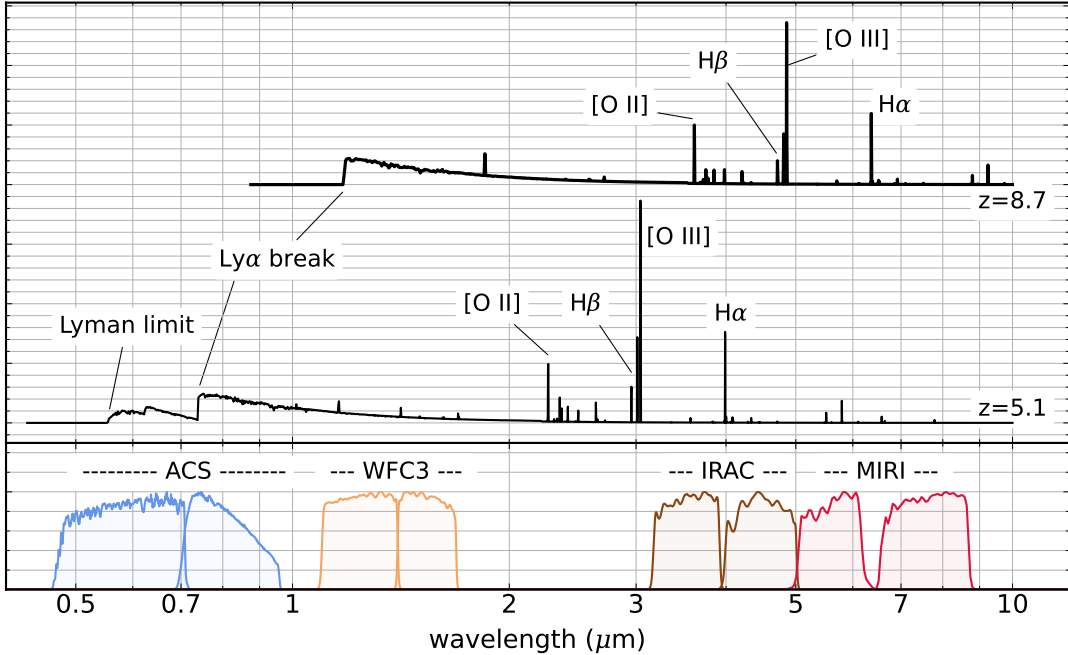


Figure 2. Illustration of galaxy spectra (in relative units of $\text{erg s}^{-1} \text{cm}^{-2} \text{\AA}^{-1}$) compared to the broad-band data for the observations in this work. The bottom panel shows the relative transmission functions for the *HST*/ACS and WFC3 filters (ACS F606W, F814 and WFC3 F125W, F160W), *Spitzer*/IRAC 3.6 μm (Ch1) and 4.5 μm (Ch2), and *JWST*/MIRI F560W and F770W. The top panel shows model spectra of star-forming galaxies at $z = 5.1$ and $z = 8.7$ (which coincidentally match two galaxies with spectroscopic redshifts in this sample). Key emission lines and features are labeled. The MIRI data probe the shape of the galaxy spectral energy distributions to 8000 \AA rest-frame, even for galaxies with $z = 9$.

$P(z)$) used for object selection). The Table also includes the amount of the integrated $P(z)$ contained between $\Delta z = \pm 0.5$ of the stated redshift, for example

$$P(z = z_c) = \int_{z_c - 0.5}^{z_c + 0.5} P(z') dz' \quad (1)$$

in bins with central redshifts of $z_c = 4, 5, 6, 7, 8,$ and 9 (see Finkelstein et al. 2022b). These integrated probabilities indicate a likelihood that a given galaxy is within the redshift bin to which it is assigned. For our analysis we rederive the photometric redshifts below (from SED modeling that includes the new 5.6 and 7.7 μm MIRI data) but include this here as we use the $P(z)$ in Table 5 as a prior likelihood on the SED fitting (discussed in Section 3 below).

Three of the galaxies in our sample have spectroscopic redshifts. This includes a previously known galaxy (ID 6811 in our catalog) with $z = 8.683$ from Zitrin et al. (2015), and two new redshifts obtained by the CEERS and WERLS collaborations from observations with Keck/DEIMOS and Keck/LRIS. The latter two sources are ID 37653 with $z = 4.899$ measured by (Stawinski et al. 2023a, in preparation) and ID 19180 with $z = 5.077$ (Stawinski et al. 2023b, in preparation). In all of these cases the spectroscopic redshifts are consistent with the photometric redshifts in Table 5, and we fix the redshift to the value of the spectroscopic redshift in our analysis of the spectral energy distributions below.

Figure 3 shows the *HST*/ACS, *HST*/WFC3, *Spitzer*/IRAC, and *JWST*/MIRI imaging for all the objects in our sample, with the objects ordered by increasing redshift (the full Figure Set of all 28 objects is available online). In all cases the galaxies show prominent “Lyman-breaks” at the location of the redshifted Lyman-limit and/or Lyman- α . In some cases, the flux density appears to be much brighter in a given pass-band compared to the adjacent band (for example, galaxy ID=12514 at $z = 7.6$ shows evidence of enhanced emission at MIRI 5.6 μm , indicative of strong redshifted H α). Figure 2 illustrates how the bandpasses are sensitive to different features in the SED of galaxies (using $z = 5.1$ and $z = 8.7$ as examples as these are similar to two of the objects with spectroscopic redshifts in our sample). We will return to these cases below when we explore constraints on the galaxy stellar populations by modeling their SEDs (Section 3).

Figure 1 shows the MIRI [5.6]–[7.7] colors for galaxies in our sample, compared to the distribution of MIRI [5.6]–[7.7] colors for all objects detected in the MIRI images. The three sources with spectroscopic redshifts are indicated with larger symbols. The high-redshift sources in our sample have MIRI [5.6]–[7.7] colors largely consistent with expectations: most objects have relatively flat ([5.6]–[7.7] ≈ 0 mag) or blue colors ([5.6]–[7.7] $\lesssim 0$ mag). This implies that in most cases the MIRI data sample the continuum of galaxies. In some cases the MIRI colors suggest very blue colors, [5.6]–[7.7] $\lesssim -0.5$ to -1 mag, roughly bounded by the bold-dashed line in the figure. The dashed line represents a photoionization model

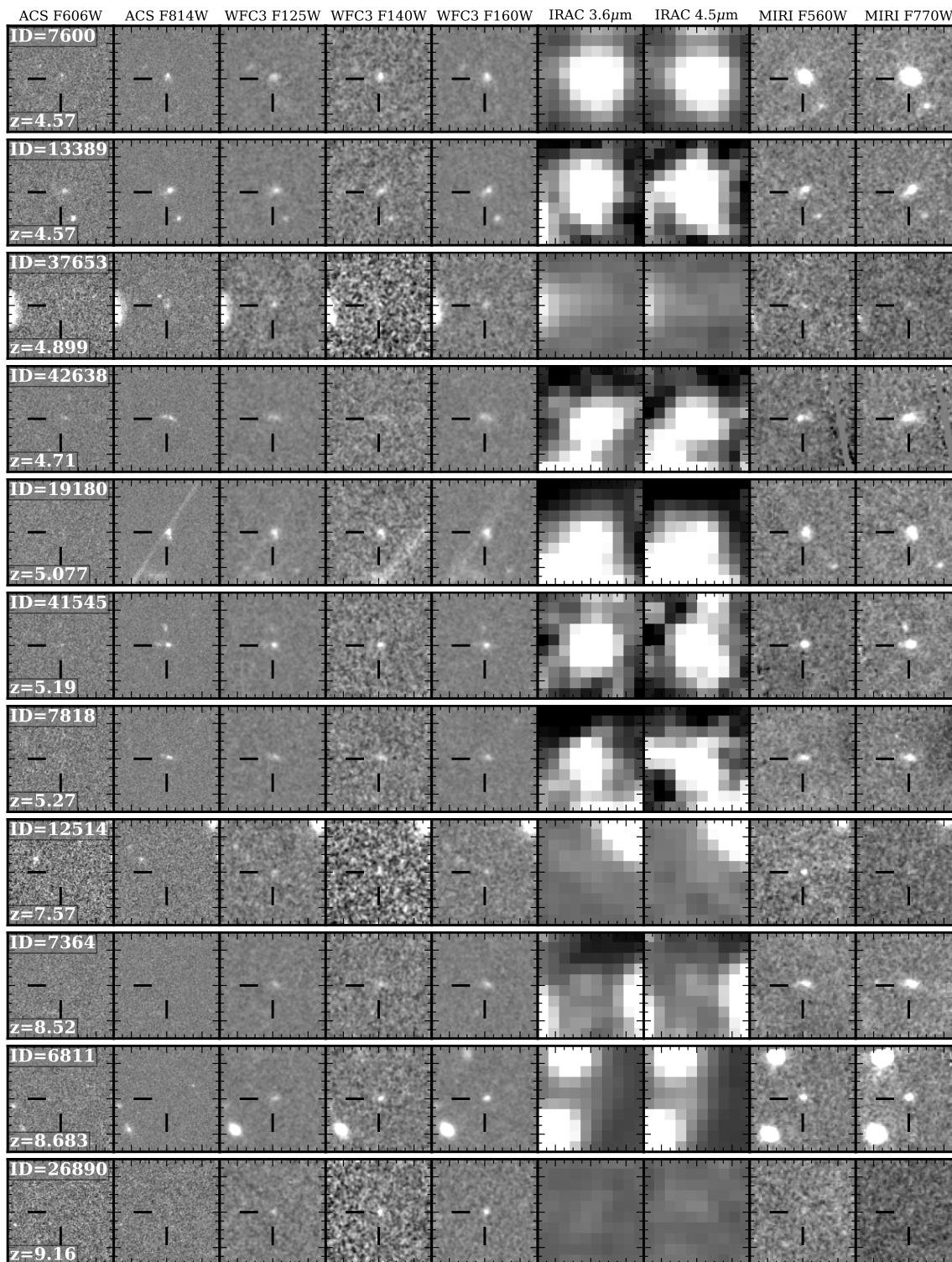


Figure 3. Montage of images of a subset of the galaxies used in this study (ordered by increasing redshift). Each row shows images for one galaxy (labeled by galaxy ID and redshift). The images are (left to right), ACS F606W, F814W, WFC3 F125, F160W, IRAC Ch1 (3.6 μ m) and Ch2 (4.5 μ m), and MIRI F560W and F770W. The images above include the three galaxies with spectroscopic redshifts (ID 37653, 19180, and 6811). The images are $6'' \times 6''$ centered on the galaxy in each bandpass, as labeled along the top row. The complete figure set (28 images) is available online.

Fig. Set 3. Montage of ACS F606W, F814W, WFC3 F125W, F140W, F160W, IRAC 3.6 and 4.5 μ m, and MIRI 5.6 and 7.7 μ m images for all galaxies in the sample (28 figures).

with a young, metal-poor stellar population (10 Myr; $0.1 Z_{\odot}$) driving strong nebular emission (set by an ionization parameter of $\log U = -2$). We will explore evidence for this interpretation below.

3. SPECTRAL ENERGY DISTRIBUTION MODELLING

We model the spectral energy distributions (SEDs) of the galaxies in our sample using stellar population synthesis models. Our goal is to test how the inferred properties of the stellar populations in the high-redshift galaxies change by including the *JWST*/MIRI 5.6 and 7.7 μm data, in particular the stellar masses and the SFRs. Previous work (pre-*JWST*) showed the MIRI data is able to recover these quantities accurately (Bisigello et al. 2017), and here we test how they improve the constraints on the stellar population parameters. This is critical for galaxies at higher redshifts, $z \gtrsim 4$, where the rest-frame optical features shift to longer wavelengths (rest-frame 4000 \AA corresponds to $>2 \mu\text{m}$), which probes light from longer-lived stars. Perhaps more problematic are the effects of nebular emission lines, which can litter the optical portion of the SED (see Figure 2). There are observations that $z > 2$ galaxies have a higher incidence of “extreme” emission lines with rest-frame EWs up to $\approx 1000 \text{\AA}$ (e.g., van der Wel et al. 2011; Tang et al. 2019; Tran et al. 2020; Boyett et al. 2022; Matthee et al. 2022; Pérez-González et al. 2022; Sun et al. 2022), consistent with inferences made from the $>3 \mu\text{m}$ colors of $z > 6$ galaxies (Smit et al. 2015; Roberts-Borsani et al. 2016; Castellano et al. 2017; Hutchison et al. 2019; Endsley et al. 2021). As the EW scales with redshift as $(1+z)$ this implies these lines have a stronger impact for high-redshift galaxies for bandpasses of fixed wavelength width (e.g. Papovich et al. 2001; Burgarella et al. 2022).

We model each galaxy by fitting *HST*/ACS and WFC3, *Spitzer*/IRAC, and *JWST*/MIRI data with stellar population models using BAGPIPES (Carnall et al. 2018). BAGPIPES is a Bayesian SED-fitting code that models the multiband photometry (flux densities) with stellar population synthesis models formed over a wide range of user-defined parameters. The code has flexibility on the type of stellar population synthesis models, star-formation history, dust attenuation, and nebular emission. It has the ability to incorporate prior knowledge on parameters. The code then computes a probability density for model parameters (i.e., posteriors) given the data by calculating a likelihood weighted by priors on the parameters, and samples the posteriors for the parameters using the MultiNest nested sampling algorithm (see Feroz et al. 2009; Carnall et al. 2018).

Table 2 lists the range of parameters considered for the SED fitting in this study. For all models we use stellar population synthesis models from Bruzual & Charlot (2003) formed with a Chabrier IMF. The table defines the parameters and their range of parameter values we explored. BAGPIPES also can incorporate priors on these parameters. In most cases we adopt uniform priors, as listed in Table 2, with two exceptions. The first is related to the nebular ioniza-

tion parameter, which controls the strength of the nebular emission features. Current evidence from spectroscopy (e.g., Oesch et al. 2015; Stark et al. 2015, 2017; Le Fèvre et al. 2015; Sanders et al. 2016, 2020; Laporte et al. 2017; Backhaus et al. 2022; Papovich et al. 2022), including recent *JWST* spectroscopy (Brinchmann 2022; Schaerer et al. 2022; Trump et al. 2022), shows that emission lines are common in star-forming galaxies at $z \gtrsim 1$ (and the strength appears to increase with increasing redshift). Therefore we fix the ionization parameter to a high, physically plausible value of $\log U = -2$ as this is representative of the values used in previous studies when fitting the SEDs of galaxies (see for example the discussion in Whitler et al. 2022). We plan to explore how variations in the ionization parameter impact the constraints on the stellar populations using future data that can include spectroscopy, e.g., from *JWST*/NIRSpec.

The other exception is for galaxies with photometric redshifts, where we use the photometric redshift posterior, $P(z)$, derived from EAZY as the prior on the redshift (see Chworowsky et al. 2022). For galaxies with spectroscopic redshifts, we force the fit to the spectroscopic redshift value listed in Table 5.

For the galaxy star-formation histories (SFHs) we test two possibilities. First, we primarily employ “delayed- τ ” models, where $\text{SFR} \propto (t/\tau) \times \exp(-t/\tau)$ for age, t , and star-formation e -folding timescale, τ . These models allow SFHs that rise with time (when $t/\tau \ll 1$) (as is expected for high-redshift galaxies, Finlator et al. 2011; Papovich et al. 2011) and for exponentially declining models (when $t/\tau \gg 1$) and these have the flexibility to broadly reproduce the evolution of galaxies over long time periods (e.g., Larson & Tinsley 1978; Tinsley 1980; Carnall et al. 2019; García-Argumániz et al. 2022).

Second, following Papovich et al. (2001) we also consider more extreme SFHs that include both the delayed- τ model (above) an early burst of stars that formed at $z_f = 100$. The reason for this is that a burst of stars formed at the earliest times has the highest mass-to-light ratio possible. As such it adds the most amount of stellar mass (at least for commonly assumed IMFs, like the Chabrier one assumed here), with the minimum impact on the observed galaxy SED. In contrast, the slowly evolving delayed- τ model provides a fit to the light from the more-recently formed stellar populations that dominate the rest-frame UV and optical light. Therefore, the UV/optical light from the stars formed in the maximally old burst can be “lost in the glare” of more recently formed stars (this is also referred to as “outshining”, Conroy 2013). The choice of $z_f = 100$ is motivated by the fact that current models expect stars to be forming by $z = 20-30$ (Barkana & Loeb 2001, and references in Section 1). The time from $z = 100$ to $z = 20$ spans less 200 Myr, during which little stellar evolution occurs for the longer-lived stars that dominate the stellar mass. By using $z_f = 100$ we allow for a “maximally old” stellar population and we constrain *any* star-formation that may have occurred at the earliest times which could have the

Table 2. Parameter Settings for BAGPIPES

Model	Parameter	Prior	Limits
Star-Formation History (1): Delayed- τ , $\Psi \propto (t/\tau)\exp(-t/\tau)$	e -folding timescale, τ / Gyr	Uniform	(0.01, 10)
	age, t / Gyr	Uniform	(0.01,15)
	stellar mass, $\log(M_*/M_\odot)$	Uniform	(5, 12)
Star-Formation History (2): Burst at $z_f = 100$ and delayed- τ model from (1)	burst age, t_{burst} / Gyr	Fixed	$t_{\text{burst}} = \text{Age}(z) - \text{Age}(z_f = 100)$
	burst stellar mass, $\log(M_*/M_\odot)$	Uniform	(0, 13)
Additional parameters for all models	dust attenuation law	...	Calzetti (2001)
	dust attenuation, $A(V)$ / mag	Uniform	(0, 3)
	metallicity, Z/Z_\odot	Uniform	(0,1)
	ionization parameter, $\log U$	Fixed	-2
	redshift [†] , z	EAZY $P(z)$	(3, 15)

[†] For galaxies with photometric redshifts the redshift prior is the posterior from the photometric redshift. For galaxies with spectroscopic redshifts the redshift is fixed at the spectroscopic redshift.

highest possible M/L (for a canonical stellar populations).³ By studying the SEDs of galaxies to longer wavelengths we can constrain the amount of light in this population. For example, Papovich et al. (2001) and Dickinson et al. (2003) found that using K -band data, galaxies at $z \sim 3$ could hide as much as 75–90% of their stellar mass in early bursts formed at $z_f = 100$. Indeed, at the risk of foreshadowing, we find that including the MIRI 5.6 and 7.7 micron data reduces the amount of possible stellar mass formed in such maximally old bursts by up to an order of magnitude (see Section 4.4).

4. RESULTS

4.1. Analysis of Galaxy SEDs

Figure 4 shows the BAGPIPES SED fits and one-dimensional (1D) posterior likelihoods for select parameters of the SED fit. The Figure shows six galaxies as an example. The online version of the *Paper* includes a Figure Set with these plots for the full sample. For each galaxy, the plots compare the SED fits with and without the MIRI 5.6 and 7.7 μm data. Tables 6 and 7 provide the medians (50th percentiles), 16th and 84th percentiles derived from these posterior likelihoods for the stellar masses, SFRs, and photometric redshifts for all galaxies in the sample, both with and without using the MIRI data, respectively.

To test the robustness of the stellar masses and SFRs derived from the BAGPIPES fits, we have refit all the galaxies in our sample using several independent SED-fitting codes (CIGALE, Boquien et al. 2019; FAST, Kriek et al. 2009, and the codes of Santini et al. 2022a and Pérez-González et al. 2008). Comparing the stellar masses and SFRs, we find they agree in the mean (with bias, $\mu \simeq 0$ dex) and an inter-method scatter of $\sigma = 0.23$ dex in stellar mass (a factor of 1.7) and $\sigma = 0.27$ dex in SFR (a factor of 1.9). This scatter is typical in comparisons of SED-fitting results (e.g., Mobasher et al. 2015). We therefore interpret the scatter as representative of the systematic uncertainties on the stellar masses and SFRs here.

In some cases adding the MIRI data has a small effect on the median values of the stellar mass and SFR, but it does tighten the allowable range of these parameters. Figure 4 panels (a) and (b) show galaxy ID 7364 (at $z = 8.1 - 8.2$) and galaxy ID 6811 (with $z_{\text{sp}} = 8.683$, Zitrin et al. 2015). These have MIRI data that support the interpretation inferred using only the *HST* and *Spitzer* data. However, in both of these cases adding the MIRI data tighten the allowed range of models, and thus improve the constraints on the stellar population parameters (this is true for the sample in general). In both cases shown here, the favored range of stellar mass and SFR are improved significantly when MIRI data are included (with improvements in the inter-68%-tile range by more than a factor of two). Below the SED fit for each galaxy, Figure 4 shows the posterior probability densities for the SFR, mass-weighted age (Age_{MW}), stellar mass, and dust attenuation. Adding the MIRI data typically produce narrower posteriors for SFR and stellar mass. This is a result of improved constraints on the dust attenuation ($A(V)$), and this forces the models to a narrower range of SFR and stellar mass. This is the case for ID 7364 and 6811.

³ A redshift of $z = 100$ is essentially “immediately” in the history of the Universe as it corresponds to an age of only $\simeq 17$ Myr after the Big Bang for the assumed cosmology. Stars are expected to form by $z \approx 20 - 30$ (Barkana & Loeb 2001 and references in Section 1), and there are reputed candidates from *JWST* imaging for galaxies at redshifts as high as $z \approx 15$ (see Section 1). Therefore, $z_f = 100$ seems to be a reasonable upper bound to ensure we capture the earliest time when stars could plausibly form. Using a lower formation redshift, $z_f < 100$, would lower the upper limit on the stellar masses that could form in the bursts as these would be younger, with lower M/L .

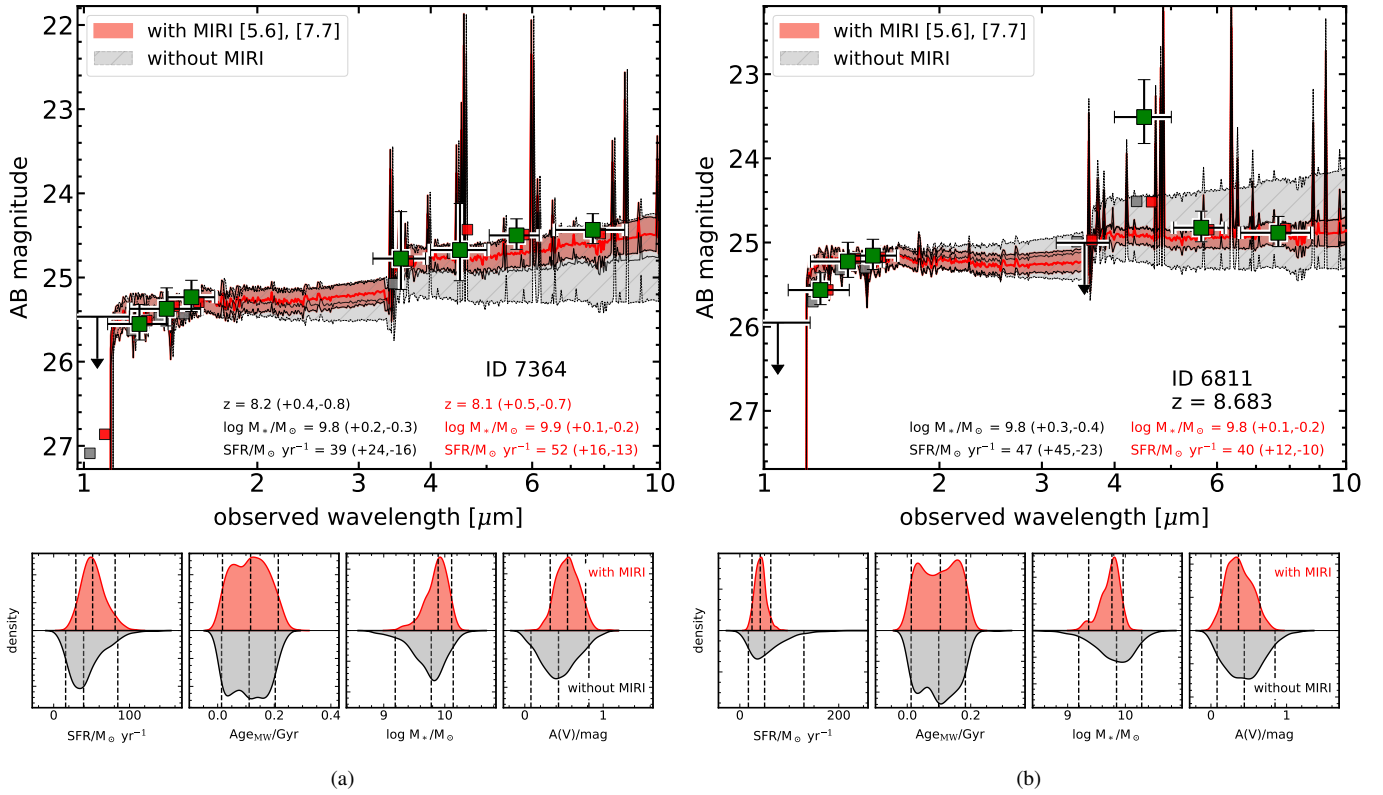


Figure 4. Examples of SED fits for galaxies in the sample. The green data points show the measured flux densities and uncertainties on the *HST*/WFC3, *Spitzer*/IRAC, and *JWST*/MIRI bands. The red-shaded regions shows the model fit to all the data points (the shaded region shows the inner-68% range of models; the solid red line shows the median). The black-shaded region shows the fit to the data points excluding the MIRI bands. The small red and grey points show the median-model photometry. The inset text gives the median and 68%-tile uncertainties on the stellar masses and SFRs inferred from the fits. Below each SED plot, the panels show the posteriors (probability density) for the SFR, mass-weighted (MW) age, stellar mass, and dust attenuation for each galaxy (using MIRI and excluding MIRI data). The dashed lines denote the 5, 50, and 95% intervals. The examples include galaxies where adding the MIRI data yields similar stellar masses and SFRs, but with tighter constraints (panels (a) and (b)). Other examples show galaxies where adding the MIRI data greatly reduces both the stellar masses and SFRs. Typically this results from contamination in the IRAC data or because of strong emission lines impacting the IRAC data (or both; see panels (c) and (d)), or because the stellar continua appear very blue (see panels (e) and (f)). The complete figure set (28 images) is available online.

Fig. Set 4. SED fits and 1D posteriors for SFRs, stellar masses, mass-weighted ages, and dust attenuation for all galaxies in the sample.

In other cases adding the MIRI data changes the interpretation of the galaxy stellar populations dramatically. Figure 4 panels (c) and (d) show galaxies with ID 19180 (with $z_{\text{sp}} = 5.077$) and ID 18441 (at $z = 6.5 - 6.6$). In both of these cases, without MIRI data the *HST* to IRAC 3.6 and 4.5 μm data implied very red rest-UV-to-optical colors, leading to high dust-attenuation values ($A(V) \gtrsim 1$ mag) with high SFRs ($\gtrsim 90 - 100 M_{\odot} \text{ yr}^{-1}$). The stellar masses in these cases are also elevated primarily because the higher dust attenuation increases the mass-to-light ratio (M/L) of the models, and therefore increases the stellar mass. Including the MIRI data changes the favored stellar population models to ones with much bluer rest-UV-to-optical colors. As a result the dust attenuation, SFR and stellar mass are decreased, by an order of magnitude in some cases (the decrease in stellar mass is more than that of the SFR, implying the *specific* SFR declines slightly as well). This impacts roughly $\approx 33\%$ of the sample

here (10 of the 28 galaxies based on our visual inspection of the SEDs and 1D posteriors, see Figure 4).

Yet in other cases, the MIRI data forces the constraints on the stellar populations to be bluer than expected based on the *HST* and *Spitzer* data. Figure 4 panels (e) and (f) show two galaxies that demonstrate these situations. In both the cases of galaxy ID 12514 (at $z = 7.4 - 7.7$) and ID 26890 (at $z = 8.8 - 8.9$) the MIRI data favor very blue UV/optical colors. In the case of galaxy 12514, there are indications that the IRAC and MIRI 5.6 μm data are boosted by the presence of strong emission lines. Having the 7.7 μm photometry favors a lower stellar continuum. As a result the SFR and stellar mass are reduced (the presence of redshifted $\text{H}\alpha$ in the MIRI F560W band is apparent even in the galaxy image in Figure 3 which shows the 5.6 μm flux density is noticeably brighter than the 7.7 μm flux density). For this reason the SED fit favors a

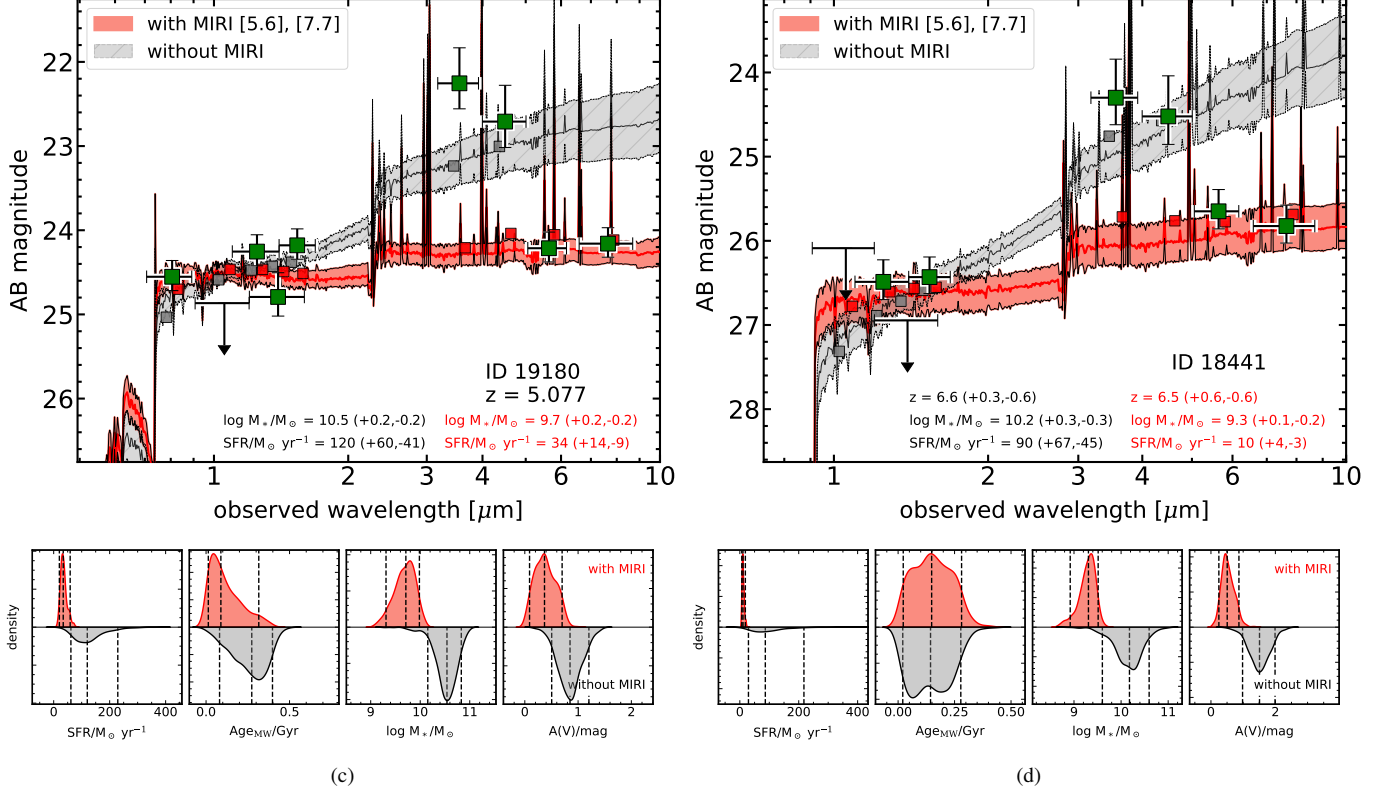


Figure 4 (continued).

slightly higher photometric redshift (to accommodate the $H\alpha$ emission in the F560W bandpass), see Section 4.2 below.

Galaxy ID 26890 is noteworthy in itself because it is the highest redshift galaxy in the sample, and because the $HST/WFC3$ -to- $JWST/MIRI$ colors are $H_{160} - [5.6] \approx -0.5$ mag, and indicative of stellar populations with very low M/L ratios. The IRAC 4.5 μm emission shows indications of enhancement, possibly owing to redshifted $H\beta + [O\text{III}]$. The MIRI data reign in the allowable range of stellar population parameters, favoring models with lower SFRs than the constraints that lack MIRI data.

Therefore, the MIRI data favor bluer rest-UV/optical colors compared to the IRAC data. In part this may have a physical explanation. At the redshifts of the galaxies under consideration, the IRAC data contain strong emission lines, including $H\beta + [O\text{III}]$ at $5 < z < 8$, $[O\text{II}] + [\text{Ne III}]$ at $7 < z < 12$, and $H\alpha + [\text{N II}]$ at $4 < z < 7$ (Labbé et al. 2013; Smit et al. 2015; De Barros et al. 2019; Roberts-Borsani et al. 2020; Endsley et al. 2021). At certain redshifts both the 3.6 and 4.5 μm bands can be both be affected (e.g., Smit et al. 2014; Roberts-Borsani et al. 2020). Without the SED fits, the models that fit the data may include both models with strong emission lines and/or models with redder colors (indicative of strong dust attenuation) or both. The models in Figure 4 show that the presence of strong emission lines in the bands augments the flux densities. This could account for part of the difference between the SED fits with and without MIRI: the MIRI data are evidence in these cases that the stellar populations have

bluer colors, and the elevated IRAC flux densities then would require strong emission line EWs to reproduce them.

However, crowding between sources in the IRAC data may be another reason for the increased IRAC flux densities. The lower angular resolution of the IRAC data can cause blending from bright, nearby galaxies, and this can lead to additional uncertainties in the flux density. As the images in Figure 3 illustrate, some galaxies (e.g., ID 19180 and 6811) have bright objects within 3 arcseconds. The light from these objects makes deblending more difficult and could potentially bias the flux-density measurements (see, e.g., Laidler et al. 2007; Skelton et al. 2014; Merlin et al. 2016). For this reason the elevated IRAC flux densities may include systematic measurement uncertainties from blended objects. In Appendix A we test for the effect of source blending by excluding objects that have any bright neighbor within $3''$ (we show that source blending does not bias our interpretation for the stellar masses nor SFRs, nor in their evolution, that we infer for the galaxy population). However this does emphasize the benefit of having data with the enhanced angular resolution available from $JWST$ imaging (for both NIRCcam and MIRI).

4.2. The Impact of MIRI on Redshifts and Implications for Emission Lines

Figure 5 compares the redshifts for the galaxies in our sample derived from our BAGPIPES fits for the galaxies excluding the MIRI data (z_{noMIRI}) and when including the MIRI data (z_{MIRI}) as a function of the prior photometric redshift

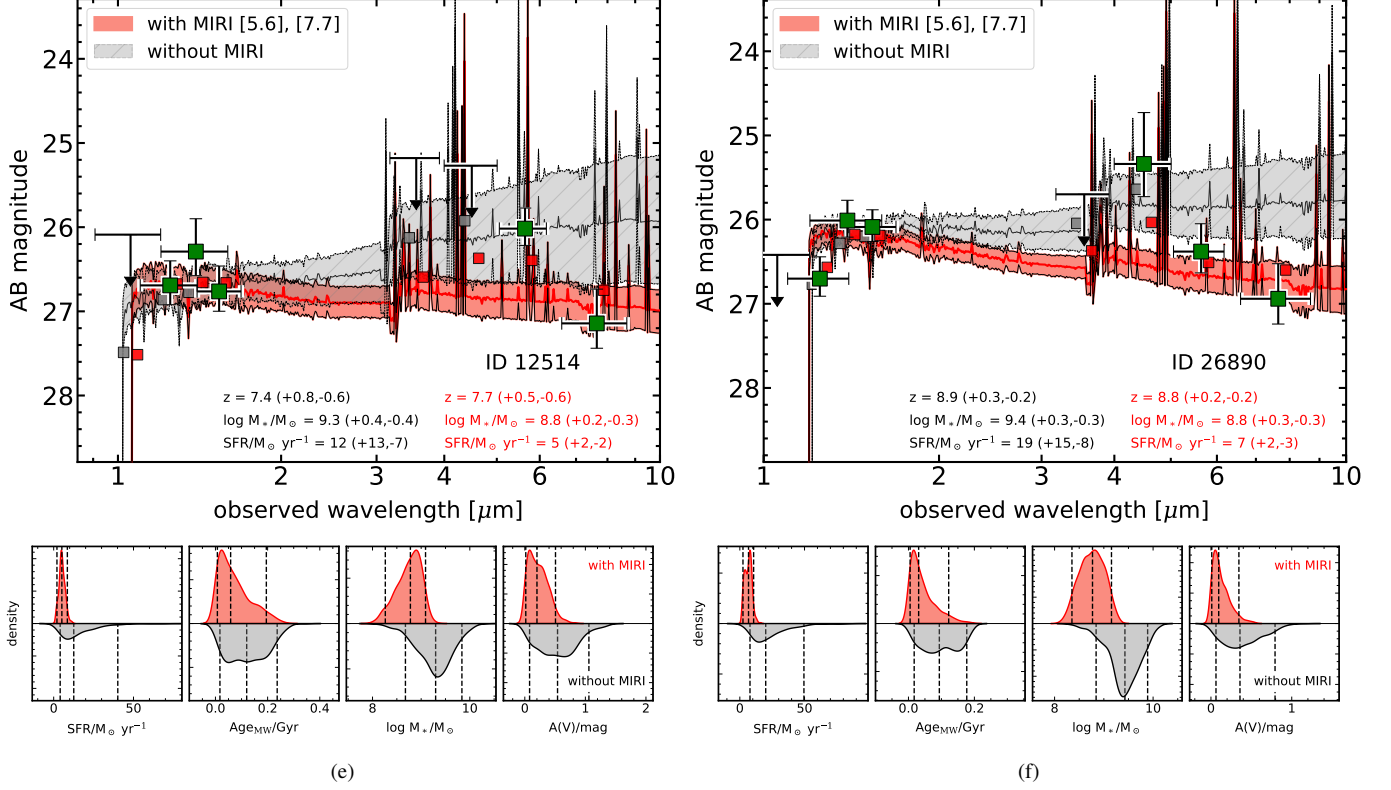


Figure 4 (continued).

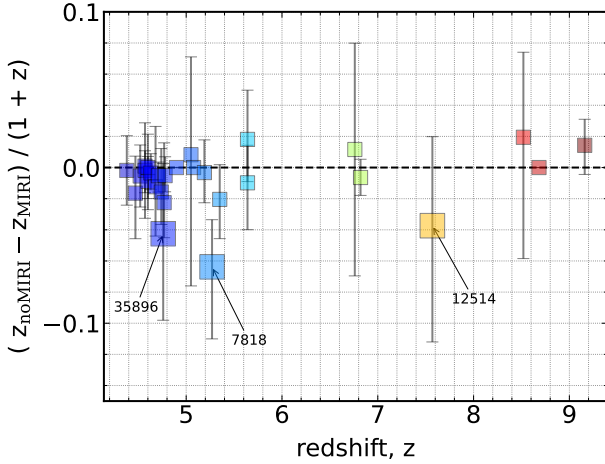


Figure 5. Comparison of the redshifts for galaxies in our sample with and without the MIRI data. The data points show the relative difference between the photometric redshifts (derived from our BAGPIPES fits) for the galaxies excluding MIRI (z_{noMIRI}) and when including MIRI (z_{MIRI}) as a function of the prior photometric redshift from Finkelstein et al. (2022b). Annotated points indicate objects with $|z_{\text{noMIRI}} - z_{\text{MIRI}}| > 0.2$. These objects indicate shifts in their photometric redshift, where at least in part this is because of nebular emission in one or more bands.

from Finkelstein et al. (2022b). For most galaxies there is good agreement. (For completeness we include all 28 galaxies in this comparison, using the photometric-redshifts even for galaxies with spectroscopic redshifts.)

In several instances we see the median redshift from the posterior shifts appreciably when including the MIRI data. Figure 5 shows three objects where the shift is greater than $\Delta z = 0.2$. In all cases the shift in the redshift probability density appears to be related to the effects of one or more emission lines in the IRAC or MIRI passbands. Figure 6 illustrates the shift in $P(z)$ from the BAGPIPES fits for these galaxies.

Two of these galaxies lie at $4 < z < 6$ (galaxy IDs 35896 and 7818). Adding the MIRI data favors having strong nebular emission in *both* of the IRAC bands. This occurs at $z \gtrsim 5$ when $\text{H}\beta + [\text{O III}]$ enters the IRAC Ch1 bandpass (at $3.6 \mu\text{m}$) and $\text{H}\alpha$ enters the IRAC Channel 2 bandpass (at $4.5 \mu\text{m}$; see Figure 2). Inspection of the galaxy SEDs (see Fig. Set. 4) shows that the IRAC-to-MIRI colors ($[3.6] - [5.6]$ and $[4.5] - [5.6]$) are blue for both of these galaxies. The BAGPIPES fits that include the MIRI data favor models in which the galaxy has strong nebular emission in the IRAC bands to account for these color. This increases (decreases) the redshift probability density at higher (lower) redshifts for these galaxies.

The remaining galaxy, ID 12514, lies at $z \approx 7.7$. Figure 6 shows the redshift probability densities for this galaxy. The MIRI F560W image (Fig. 3 shows evidence of “boosted” flux

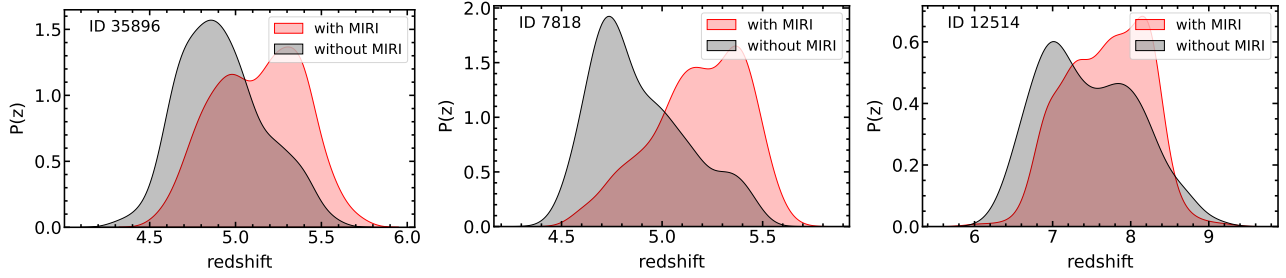


Figure 6. Comparison of redshift posterior probability densities, $P(z)$, derived from the BAGPIPES fits to three of the galaxies in the sample (as labeled). These three galaxies each have a change of more than 0.2 between the median redshift when including the MIRI F560W and F770W data in the fit versus when they are excluded. For the case of galaxy IDs 35896 and 7818, the IRAC–MIRI colors are blue, indicating redshifted emission lines (likely $H\beta$ + $[O\text{ III}]$ and $H\alpha$) inhabit both IRAC bands (while the MIRI data probe the galaxy continua). In the case of galaxy ID 12514, the MIRI F560W band clearly shows boosted emission, likely from redshifted $H\alpha$ at $z = 7.6$ – 8 .

compared to the MIRI F770W image, where the MIRI color is $[5.6] - [7.7] = -1.1 \pm 0.3$ mag, see Table 5). The most likely explanation for this boosted emission appears to be from redshifted $H\alpha$ + $[N\text{ II}]$ at $z = 7.6$ – 8.0 in the MIRI F560W bandpass (see Fig. 4). The strength of the flux in the F560W bandpass decreases the probability density for redshifts with $z \lesssim 7$ as these would place $H\alpha$ at wavelengths shorter than covered by the bandpass (see Figure 2).

Therefore, nebular emission lines appear to be responsible for the cases where there are larger shifts in the photometric redshift solutions. However, these cases are generally exceptions. For most galaxies in the sample the redshift posteriors are consistent, where Fig. 5 shows the differences are negligible in median redshifts with and without including the MIRI data. We expect that many (even most) of the galaxies in the sample also exhibit strong emission lines given the preponderance of evidence from other galaxies at these redshifts (see Section 4.1) and by inspection of the SEDs in Figure 4. In these cases adding the MIRI data supports the redshifts, either because the emission lines make less of an impact on the redshift likelihoods or because the MIRI data reinforce them.

4.3. The Impact of MIRI on the Stellar Masses, Dust Attenuation, and SFRs

Figure 7 compares the stellar masses and SFRs derived for the galaxies in our sample using the simple delayed- τ models with BAGPIPES for the case where we include the MIRI F560W and F770W data and when we exclude it. In general, including the MIRI data *reduces* the stellar masses and SFRs for the galaxies.

We study the offsets in stellar mass and SFR for our galaxies in two redshift bins, $4 < z < 6$ and $6 < z < 10$, where the median offsets in stellar mass and SFR are indicated in the Figure as large rectangles, and are listed in Table 3. Formally, the offsets in stellar mass are $\Delta \log(M_*/M_\odot) = 0.25$ dex for $4 < z < 6$ and 0.38 dex for $6 < z < 10$. The inter-68%-tile intervals are 0.28 and 0.44 dex, respectively (estimated using the median absolute deviation, σ_{NMAD}). For the SFRs the offsets are $\Delta \log(\text{SFR}/M_\odot \text{ yr}^{-1}) = 0.15$ dex for $4 < z < 6$

Table 3. Offsets in Stellar Mass and SFRs for $4 < z < 10$ galaxies when including the MIRI F560W and F770W data

Sample	Stellar Mass offsets		SFR offsets	
	Median	Scatter	Median	Scatter
$4 < z < 6$	0.25 dex	0.28 dex	0.15 dex	0.12 dex
$6 < z < 10$	0.38 dex	0.44 dex	0.29 dex	0.27 dex

NOTE—The quantities with the subscript “noMIRI” denote values derived without the MIRI data. Quantities with the subscript “MIRI” denote the values derived with the 5.6 and 7.7 μm MIRI data. The scatter is the inter-68-percentile interval derived from the median absolute deviation.

and 0.29 dex for $6 < z < 10$, with an inter-68 percentile interval of 0.12 dex and 0.27 dex, respectively. Because the impact of MIRI is larger on the stellar mass than the SFR, the specific SFRs will be reduced by approximately by $\Delta \log \text{SFR} - \Delta \log M_* \approx 0.1$ dex (see Table 3).

The reasons for the offsets are similar to that discussed for the individual galaxies in Section 4.1. Including the MIRI data generally favors stellar populations with bluer rest-UV/optical colors, with lower M/L ratios. This forces the constraints to lower stellar-mass models. For the SFRs, because the colors are bluer, there is less dust attenuation favored in the models, which lowers the SFRs compared to models with higher dust attenuation (at fixed *observed* galaxy luminosity). The MIRI data also remove some of the degeneracy between models with redder stellar populations versus those with strong emission lines impact select bands. These have the combined effect of favoring lower stellar masses and SFRs when including the MIRI data.

There is significant scatter in the offsets of stellar mass and SFR for individual objects. In Figure 7 the error bars on the large rectangles show the inter-68-percentile range (i.e.,

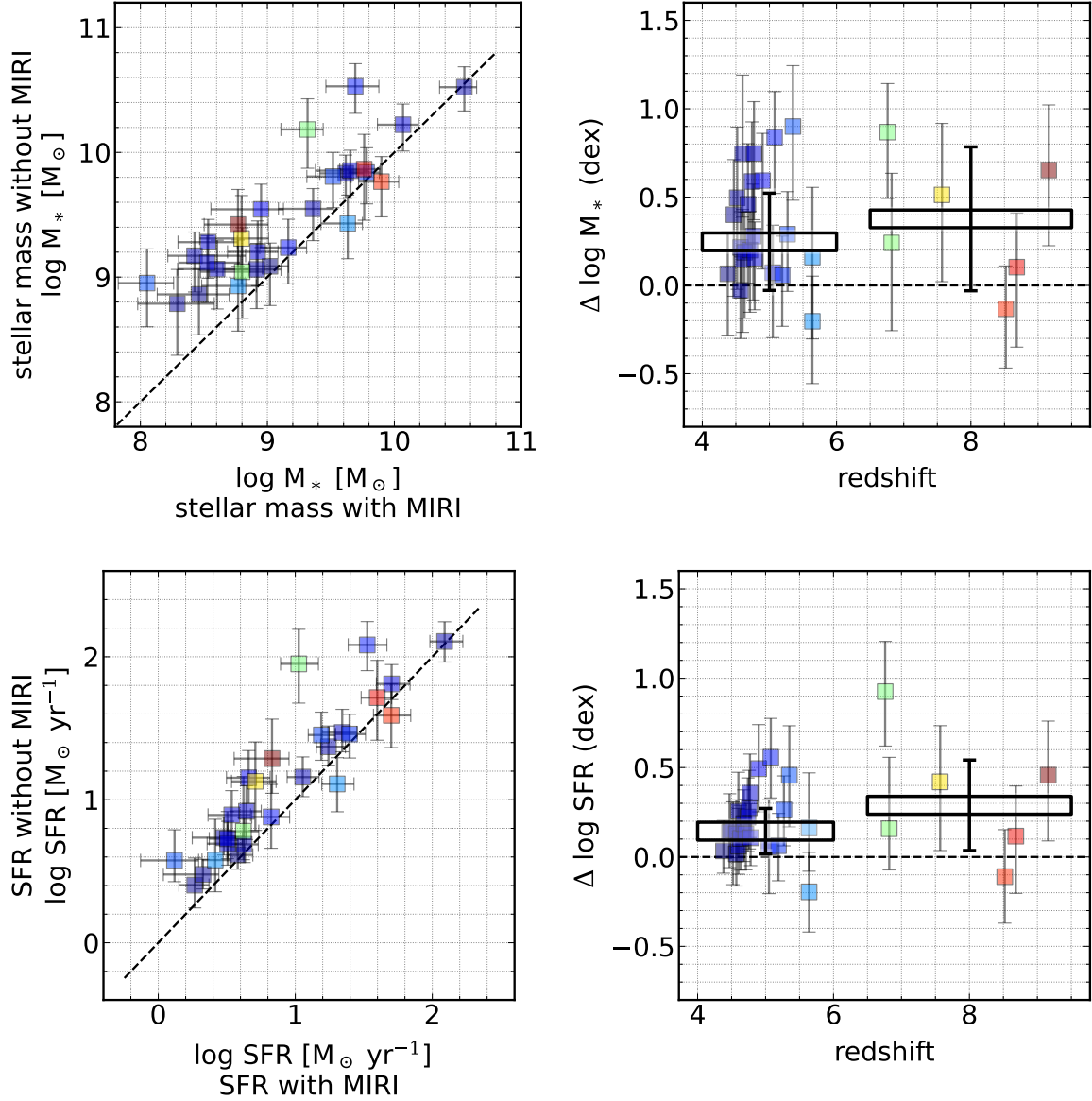


Figure 7. Comparison of stellar masses and SFRs derived from the SED modeling for galaxies including the MIRI F560W and F770W data and without the MIRI data. The top set of panels show the comparison for the stellar mass. The bottom set of panels show the comparison for the SFR. In each row the left panel shows the direct comparison, where the dashed line shows the one-to-one relation. The right panel shows the logarithmic difference, defined as $\Delta \log M_*^{\text{with MIRI}} - \log M_*^{\text{without MIRI}}$ (similarly for the SFR). The symbols are color-coded by redshift (using the right panel). In the right panel the large rectangular boxes (and error bars) show the median value (and scatter) in two bins of redshift ($4 < z < 6$ and $6 < z < 10$). The values for these are given in Table 3. Adding the MIRI data generally lowers the SFRs and stellar masses of these galaxies (though the scatter is significant). The median offset is larger for galaxies at higher redshifts.

the difference between the 16–84 percentiles) for both the $4 < z < 6$ and $6 < z < 10$. For some galaxies the offsets are insignificant, with $\Delta \log M_* \approx 0$ and $\Delta \log \text{SFR} \approx 0$. Two of these galaxies are shown in Figure 4 (IDs 7364 and 6811; others are available in Fig. Set. 4). In these cases the MIRI data tighten the existing constraints on the derived stellar masses and SFRs, reducing the uncertainties (by 0.1–0.2 dex in stellar mass and by 0.3 dex in SFR). In other words, for some cases the MIRI data support the range of stellar popula-

tion parameters favored by the fits to the *HST*/ACS + WFC3 and *Spitzer*/IRAC data, but the MIRI data improve the accuracy of the measurements, typically by a factor of order two.

In other cases the MIRI data dramatically change the interpretation of the galaxies. This was noted above for galaxies 18441 and 19180 (Section 4.1 and Figure 4), where adding the MIRI data reduce the stellar mass and SFRs substantially. Figure 7 shows that this is typically the case, where the MIRI data decrease the average stellar mass and SFR for galaxies

in our sample, typically by a factor of order two. We will explore the implications this has on the evolution of the galaxy stellar-mass density in Section 5.

4.4. The Impact of MIRI on the Inferred Star-Formation History (and the Mass Formed in Bursts)

Arguably, one of the most extreme star-formation histories imaginable is the case where a galaxy forms in either one burst at $z_f \rightarrow \infty$, or (slightly less extreme) in a series of bursts extending back to that time. When a burst forms, the stellar population immediately begins aging. A burst at $z_f = \infty$ has the oldest possible age at any subsequent time, and the smallest amount of light (at a given mass), and therefore it would have a maximal M/L at any observed epoch. As the stellar population ages, its colors also become redder. For all these reasons, it is conceivably possible to hide significant amounts of stellar mass formed at earlier times (this is the “outshining” problem, e.g., Papovich et al. 2001; Dickinson et al. 2003; Papovich et al. 2006; Finkelstein et al. 2010; Pforr et al. 2012; Conroy 2013).

One advantage of focusing on galaxies at high redshifts is that the amount of *time* for discrete episodes of star-formation (i.e., many individual bursts) is small given the age of the Universe (the Universe has an age of 1 Gyr at $z = 5.7$ and 500 Myr at $z = 9.6$ for the adopted cosmology). This is shorter than the lifetimes of stars of spectral type A and later. The short age of the Universe, combined with longer wavelengths probed by the MIRI 5.6 and 7.7 μm data allow us to place tighter constraints on the mass from earlier bursts in high redshift galaxies than has been possible previously.

We explored the possibility that such an early burst could contribute stellar mass to the galaxies in our sample, and how the *JWST*/MIRI data can improve the constraints on this population. We used the SED fits to the galaxies in our sample using a star-formation history that include both the delayed- τ model (as in Section 3 above) and the burst of stars formed at $z_f = 100$. The details of the other model parameters are listed in Table 2.

To quantify the amount of allowed stellar mass formed in the burst for each galaxy, we use the Bayesian Information Criterion (BIC, Bailer-Jones 2017). The BIC provides a criterion for model selection in the case that one introduces a model with an additional parameter (in our case we are selecting between between two models, one with a star-formation history that has a delayed- τ model only, and one with both the delayed- τ model and an early burst at $z_f = 100$). When comparing the two models, the BIC applies a penalty term for the additional parameter (to determine if the additional parameter improves the fit, or is overfitting the data).

We use the BIC defined as (e.g., Buat et al. 2019),

$$\text{BIC} = \chi_0^2 \times k \ln N, \quad (2)$$

where χ_0^2 is the minimum chi-squared from the SED-fitting, k is the number of independently fitted parameters (we use $k = 7$) and N is the number of data points ($N = 8$ or 10 , depending on if the MIRI [5.6] and [7.7] data are included or not).

Our goal is to quantify the upper limit on the stellar mass formed in an early burst that could exist in our galaxies. To do this, we select models with bursts ($z_f = 100$) that are not excluded by the BIC criteria. That is, for a given galaxy we identify all models that satisfy $\chi^2 \leq \text{BIC}$, where the BIC is defined in Equation 2, and χ^2 is the fit for a given model (this is similar to the approach adopted by Buat et al. 2019). For each galaxy, we select the model with the highest stellar mass in the $z_f = 100$ burst from the subset of models that satisfy the BIC. We then take this as upper limit on the stellar mass permitted in the burst. Comparing this upper limit on the stellar mass formed in bursts to the range of stellar masses from the fits we find that the limiting stellar mass from models that satisfy the BIC criteria corresponds roughly to a 99.7% upper limit on the mass (i.e., the values we report correspond approximately to a 3σ upper limit on the stellar mass). Tables 6 and 7 list the upper limit on the stellar mass in the burst component for all galaxies in the sample for the case that we include and exclude the MIRI data, respectively.

Figure 8 shows example SED fits for galaxies in our sample, both with and without the bursts, for the both the cases that we include and exclude the MIRI 5.6 and 7.7 μm data. The complete figure set (28 images) is available online. The examples shown in the Figure include a galaxy where the IRAC data are bright relative to the MIRI data (ID 18441). In this case, without the MIRI data the allowed stellar mass in the burst can reach $\log M_*/M_\odot = 11.0$, but adding MIRI reduces this by nearly an order of magnitude. For galaxy ID 7364, the MIRI data favor red IRAC-to-MIRI colors. Nevertheless, because the MIRI data constrain the models at longer wavelengths, they also lower the amount of stellar mass allowed in the burst: without the MIRI data the burst can include $\log M_*/M_\odot = 10.9$; when MIRI data are included the mass in the burst declines by 0.3 dex (a factor of two). For galaxy ID 6811, the MIRI data show that because they constrain the SED at longer wavelengths, the amount of stellar mass allowed in the burst is reduced by a factor of 0.6 dex (nearly a factor of five).

Therefore, the addition of the MIRI F560W and F770W data reduce the amount of stellar mass that can form in early bursts. Figure 9 shows the change in stellar mass for the case that the star-formation histories include only delayed- τ models (labeled “no burst” in the figure) compared to when an early burst of star formation at $z_f = 100$ is included (labeled “allowed in burst”) in the figure. Figure 9 shows the results for both the case that the MIRI data are excluded (top row) and when the MIRI data are included (bottom row). For the fits that lack MIRI data, the amount of stellar mass allowed in the burst is nearly an order of magnitude higher than constrained in the delayed- τ models: in this case the median differences in the log of the stellar mass of the models with early bursts and those with only delayed- τ models is 0.9 dex at $4 < z < 6$ and 1.1 dex at $6 < z < 9$. For the fits that include the MIRI data, the amount of stellar mass allowed in the bursts is significantly reduced: the median differences in

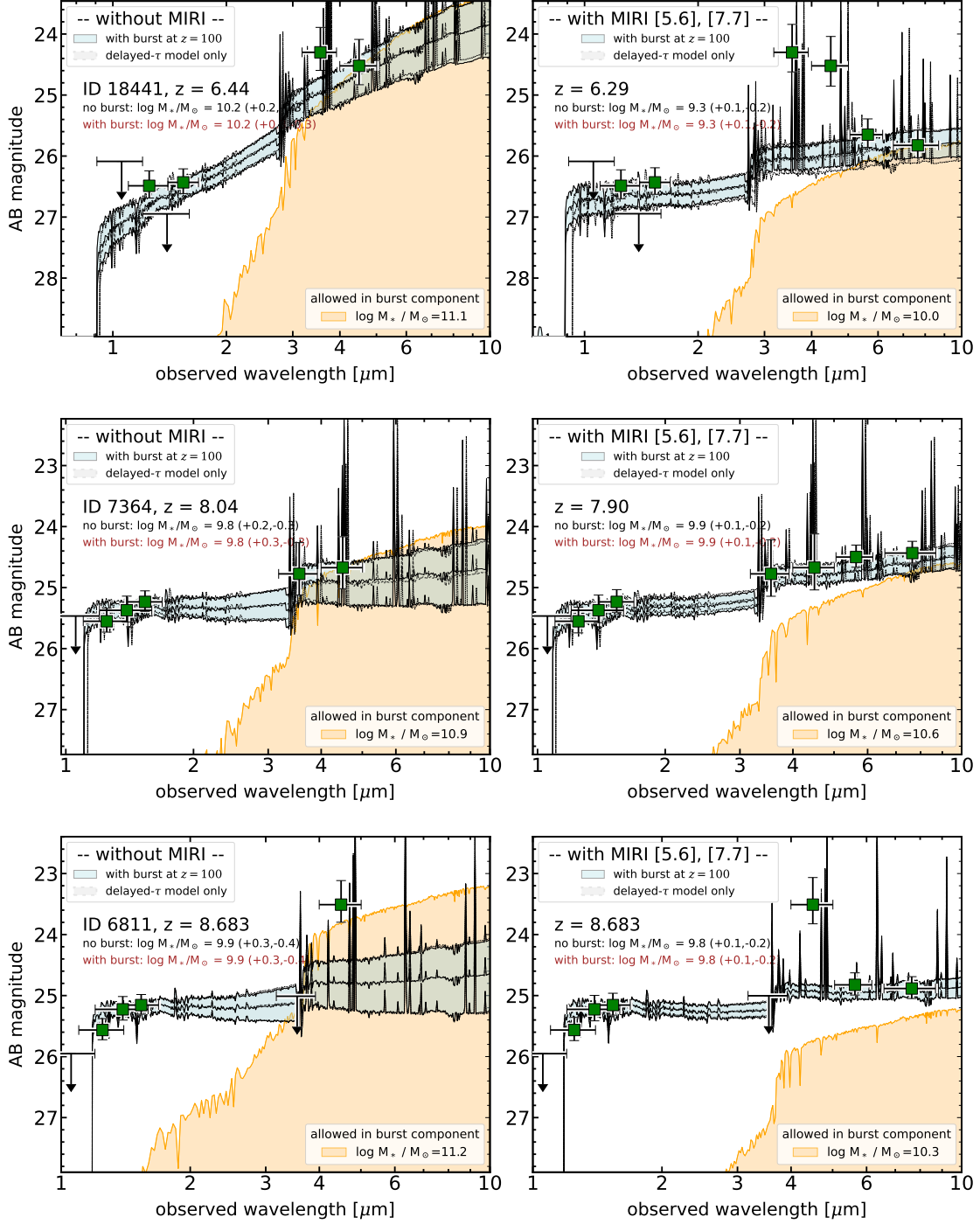


Figure 8. Example fits to SEDs for the galaxies in our sample, comparing the results from fits that include an early burst of star-formation at $z_f = 100$. Data points and upper limits have the same definitions as in Figure 4. In each panel, the shaded regions show the stellar population fit to the SED using the total model (cyan-shaded = delayed- τ plus the burst) and delayed- τ model only (gray-shaded, these are identical to those in Figure 4; there is almost no difference between the cyan- and gray-shaded models). The tan-shaded region shows the light permitted in the burst component. The labels indicate the amount of stellar mass in each component. Each row shows the results for one galaxy, where the Left panel shows the results that exclude the MIRI F560W and F770W data, and the right panel shows the results including the MIRI F560W and F770W data. The complete figure set (28 images) is available online.

Fig. Set 8. SED fits including the MIRI data and excluding the MIRI data for all galaxies comparing the fits with and without bursts at $z_f = 100$.

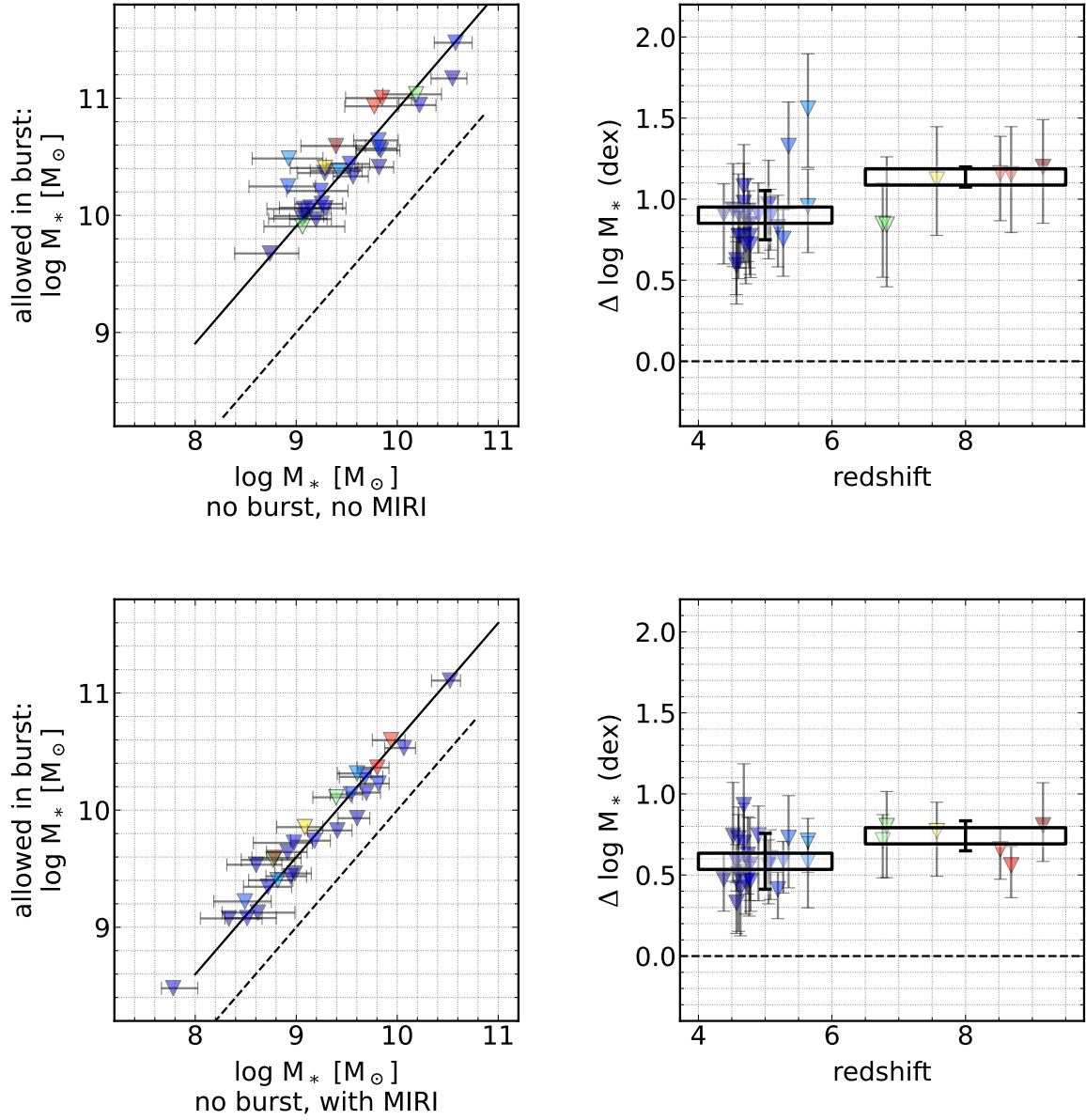


Figure 9. Comparison of stellar masses derived for galaxies with and without early bursts (at $z_f = 100$). The top row shows the results that lack MIRI data. The top-left panel shows the stellar masses derived from the delay- τ models only (labeled “no burst”) compared to the models that include the burst (labeled “allowed in burst”). The top-right panel shows the difference between the stellar masses as a function of redshift. The bottom row shows the same results for the galaxies including the MIRI data. In the left panels, the dashed lines show the one-to-one relation and the solid lines show the median offsets. In the right panels, the large rectangles show the medians in two bins of redshift ($4 < z < 6$ and $6 < z < 9$) these are given in Table 4. Adding the MIRI data reduces the amount of stellar mass allowed in the burst components.

Table 4. Ratio of the stellar mass allowed in models that include an early burst of star-formation (at $z_f = 100$) to those that include only a delayed- τ model.

Sample	$\log M_*(\text{with burst}) - \log M_*(\text{no burst})$			
	with MIRI data		no MIRI data	
	Median	Scatter	Median	Scatter
$4 < z < 6$	0.59 dex	0.16 dex	0.87 dex	0.23 dex
$6 < z < 10$	0.69 dex	0.04 dex	1.11 dex	0.13 dex

NOTE—The values labeled “with burst” denote the upper limit on the stellar mass for models that include bursts. The values labeled “no burst” denote the stellar masses for models that assume only a delayed- τ star-formation history. The values “with MIRI” include the 5.6 and 7.7 μm flux densities from MIRI.

this case 0.6 dex at $4 < z < 6$ and 0.7 dex at $6 < z < 9$. These values are listed in Table 4.

5. DISCUSSION

5.1. On the Colors, Stellar Masses, and Nebular Emission in Early Galaxies

One of main findings in this paper is that the MIRI data favor bluer colors in galaxies at $4 < z < 9$. Figure 10 shows this by comparing the relative SED for each galaxy, both in the case of including the MIRI data and without the MIRI data. Including the MIRI data reduces the derived rest-frame I -band light by approximately $\Delta m_{1600} - I \approx 0.4$ mag. Inspecting Figure 10 this appears to result from many galaxies favoring bluer SEDs when the MIRI data are included. In other words, without the MIRI data, the SED is unconstrained at longer wavelengths, and this allows for a greater range of SED shape (where the median favors a solution which on average is redder). Adding the MIRI data shifts the likelihood to bluer populations for many galaxies. This has a major impact on the implied M/L , as the blue rest-frame colors implies younger ages, lower dust attenuation, or both. The fact that adding the MIRI data makes the galaxies bluer largely explains the differences in the derived stellar masses and SFRs observed in Figure 7, where adding the MIRI data lower the stellar masses and SFRs compared what the models favor when the MIRI data are excluded.

Therefore, our interpretation of the MIRI data is that galaxies at high redshifts ($z > 4$) are bluer than inferred from previous studies. This adds to other studies that find that galaxies at high redshifts must have (very) blue colors. Studies from the pre-*JWST* era have argued that galaxies at $z > 4$ show indications of declining (i.e., steepening) UV spectral slopes with increasing redshift (e.g., Bouwens et al. 2012; Finkelstein et al. 2012; Wilkins et al. 2016; Bhatawdekar & Conselice 2021). These conclusions have been reinforced by early *JWST* imaging that shows very blue colors among UV-selected galaxies (e.g., Nanayakkara et al. 2022; Topping

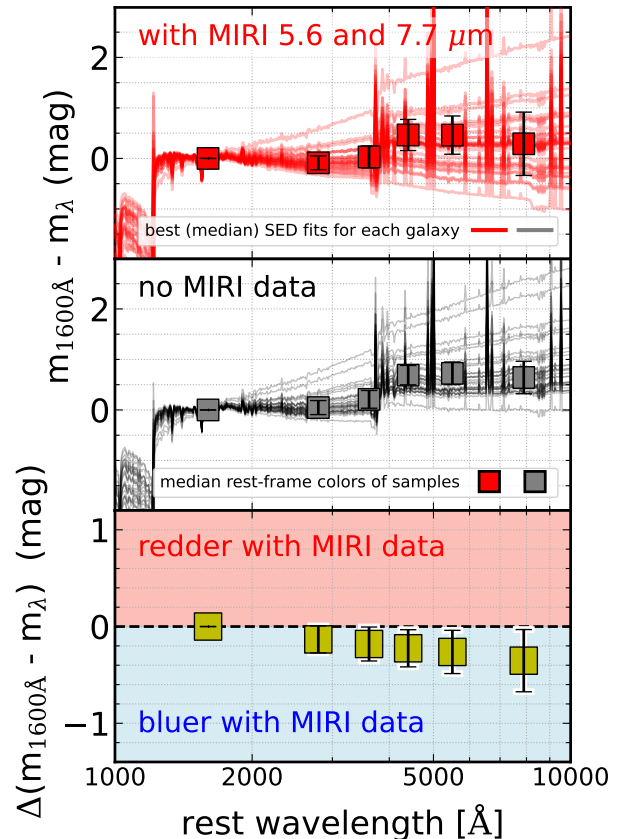


Figure 10. Comparison of median, relative SED for each galaxy, both for the case that MIRI data are used (top panel) and when the MIRI data are excluded (middle panel). The individual lines are the median SED model fit to each galaxy in the sample, shifted to the rest-frame. The large data points show the median rest-frame magnitude at 1600 Å, 2800 Å, and $U, B, V,$ and I . The error bars show the scatter in the sample. All models have been normalized to the 1600 Å magnitude (which accounts for the lack of scatter at that wavelength). The bottom panel shows the difference in color (Δm) between the models with and without the MIRI data (the error bars show the range of the 16th-84th percentiles of the sample). The change in the color at the reddest wavelengths probed (about the rest-frame I -band) corresponds to a $\Delta m \approx 0.4$ mag

et al. 2022). We find here that including the MIRI 5.6 and 7.7 μm data show strong evidence that the stellar populations are very blue in their rest-frame UV-to- I -band colors, seemingly more so than inferred from these previous studies (as in some cases the galaxies in our sample are identical to those in these other studies). Therefore, the MIRI data favor lower stellar masses and lower SFRs in distant galaxies.

Adding the MIRI data also changes the interpretation of the strength of nebular emission in the galaxies in the sample. Many of the galaxies show red colors between the *HST*/WFC3 and *Spitzer*/IRAC data (Figure 4). In the absence of MIRI data, the SED fitting interprets these colors as a combination of higher dust obscuration, older ages, and

strong nebular emission. This has been reported previously for individual galaxies and for stacked samples at $z > 6$ (e.g., Castellano et al. 2017; Stark et al. 2017; De Barros et al. 2019; Hutchison et al. 2019; Endsley et al. 2021; Stefanon et al. 2022). The fact that *without* the MIRI data the models allow for higher dust obscuration and older stellar populations increases the M/L and the stellar masses. The higher dust obscuration also leads to higher SFRs. However, including the MIRI data changes this interpretation for the galaxy population. Nebular emission lines appear to be the primary explanation for the red *HST*/WFC3 to *Spitzer*/IRAC colors (while there are some galaxies where the MIRI data does not change [e.g., galaxy IDs 6811 and 7364 in Figure 4] this does not change the main result *in general*). This means (1) the nebular emission lines for high redshift galaxies must be strong and (2) the stellar populations are blue. Early *JWST* results show emission lines remain strong in high-redshift galaxies and impact the reddest ($4-5 \mu\text{m}$) bandpasses in NIRCcam (e.g., Endsley et al. 2022; Giménez-Arteaga et al. 2022; Santini et al. 2022b; Topping et al. 2022; Whitler et al. 2022). The MIRI data appear necessary to extend the rest-frame wavelength coverage to $>7000 \text{ \AA}$, past the strongest of the nebular emission features in the rest-frame optical.

5.2. Implications for Early Star-Formation and Stellar Masses in Galaxies

The difference between the delayed- τ star-formation history and the model that includes bursts, while simplistic, arguably span the gamut of available star-formation histories of galaxies. Simulations show that galaxies experience many discrete bursts, but when averaged over long time baselines the evolution is mostly smooth (e.g., Diemer et al. 2017; Iyer et al. 2019; Leja et al. 2019). Therefore the smoothly evolving delayed- τ model represents the slowly evolving evolution of galaxy star-formation histories. This can reproduce the bluest colors (and lowest M/L) of the stellar population. Of course, galaxies can experience a host of stochastic bursts through changes in gas accretion or events that can sudden changes in the star formation (as a result of mergers, e.g., Kartaltepe et al. 2022, or the sudden onset of strong feedback from an AGN, e.g., Wagner et al. 2016). “Bursts” of star-formation from these events will add stellar mass, but if these occur at $z < 100$ then will be younger, and will have M/L lower than a model with a burst at $z_f = 100$. As such, the models with a burst at $z_f = 100$ have the maximum M/L and the oldest possible ages for a stellar population at the observed redshift of each galaxy. Therefore the models with this burst represent a maximum stellar mass possibly formed in these galaxies.

Our results show that including MIRI reduces the amount of stellar mass allowed in these models, by an order of magnitude in some cases. In itself this is interesting as nearly all galaxies show no direct evidence for such early star-formation. Comparing the *median* stellar masses of galaxies when fit by the delayed- τ models only and those with the delayed- τ models and the early burst at $z_f = 100$ shows they differ by $\text{median}(\Delta M_*) \approx 0.1$ dex (see the plots in Figure 8).

We find no convincing cases in our sample where the galaxies *require* a burst at $z_f = 100$ to better fit their SEDs. This would imply that galaxies do *not* experience early bursts of star-formation (or at least such bursts do not form sufficient mass that we require them).

Part of our findings could be impacted by biases. First there is selection bias: all the galaxies studied here were selected in *HST*/WFC3 data, and therefore required some rest-frame UV emission above the *HST*/WFC3 detection limit. It will be important to test for objects in, for example, future *JWST*/NIRCam-selected populations show evidence for early bursts (especially *JWST*-selected samples that lack *HST* counterparts, Glazebrook et al. 2022; Pérez-González et al. 2022). Second, very recent work shows evidence for older stellar populations in the spatially resolved colors of $6 < z < 9$ galaxies (Giménez-Arteaga et al. 2022). As these issues become better constrained, then the ages of the stellar populations in distant galaxies could begin to inform us about when galaxies first form stars (see Whitler et al. 2022).

5.3. Implications for Galaxy Growth

The question of how much mass is contained in galaxies is related to the integral of the galaxies’ star-formation histories. This is important because it contains the integrated record of how rapidly galaxies acquire their baryons, and how efficiently they convert these into stars. This has already been discussed as an impossibly early galaxy problem, where galaxies may have acquired too much stellar mass: in typical *JWST* surveys galaxies should have less stellar mass than a few times $10^{11} M_\odot$ (Behroozi & Silk 2018; Boylan-Kolchin 2022).

The effect of adding the MIRI data already show that stellar masses and SFRs derived for galaxies tend to be overestimated. The median offsets for the galaxies in our sample are 0.15 dex at $4 < z < 6$ and rise to ≈ 0.3 dex at $6 < z < 9$ (Figure 7 and Table 3). Assuming that these (median) offsets apply to previous estimates of galaxy stellar masses, then it implies that measurements of the cosmic SFR density (SFRD, which is the average SFR in all galaxies per co-moving volume element) are similarly biased to higher values at these redshifts.

Figure 11 shows the impact of these lower SFRs on the cosmic *stellar-mass density*, ρ_* . Firstly, the figure shows ρ_* derived from the integral of the SFRD for two empirical models calibrated against measurements from the literature (Madau & Dickinson 2014; Finkelstein 2016). Finkelstein (2016) shows that these models are consistent with a compilation of measurements of ρ_* from the literature at $4 < z < 10$ prior to the launch of *JWST*, (Oesch et al. 2014; Duncan et al. 2014; Grazian et al. 2015; Song et al. 2016). The thick line in Figure 11 labeled “MIRI corrected” shows the empirical model of Finkelstein corrected by the offsets of the SFRs derived in Table 3. To derive these corrections we have interpolated the results from Table 3 assuming median redshifts of $z = 5$ and 8 for the derived offsets in the two redshift bins. Parenthetically, although we use the offsets derived from the SFRs, using those for the stellar masses changes the results

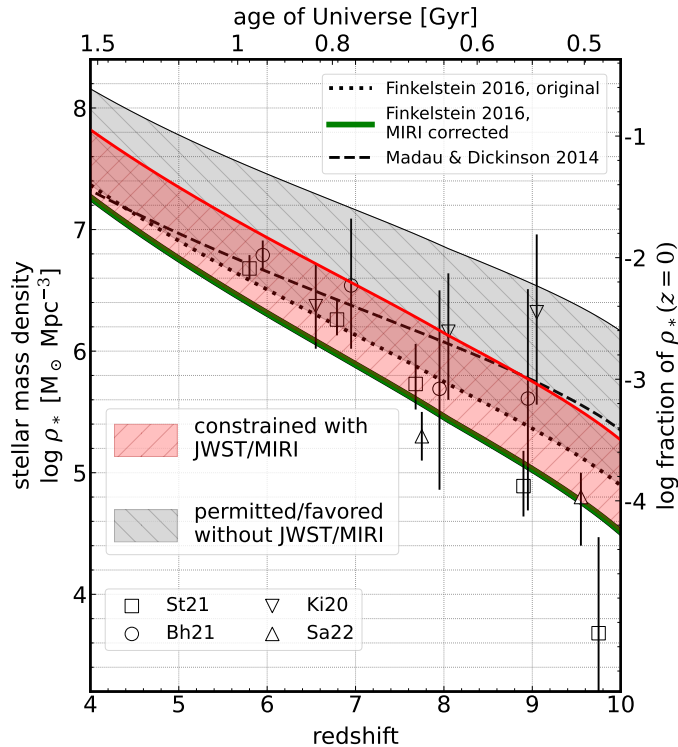


Figure 11. Evolution of the cosmic stellar mass density, ρ_* , in galaxies from $4 < z < 10$. The lines show pre-*JWST* constraints from Finkelstein (2016) and Madau & Dickinson (2014). The data points show recent measurements of ρ_* at $z > 6$ from the literature (Kikuchi et al. 2020 [Ki20], Bhatawdekar & Conselice 2021 [Bh21], Stefanon et al. 2021 [St21], Santini et al. 2022a [Sa22]), which largely follow the pre-*JWST* constraints. The shaded regions show maximally allowable stellar mass density assuming galaxies experience a burst at $z = 100$ followed by “normal” star-formation. Constraints lacking *JWST/MIRI* coverage to rest-frame $1 \mu\text{m}$ allow for a stellar mass density that is up to 0.8 dex higher at $z = 4$ and 1.4 dex higher at $z = 10$. Including *JWST/MIRI* 5.6 and 7.7 μm data lowers the maximum allowed by up to a factor of 5.

by ≈ 0.1 dex). We note, however, that because the *MIRI* data imply offsets in the SFRs of galaxies, the similarly lower values of the cosmic SFRD at $z > 4$.

Secondly, the *MIRI* data improve the constraints the amount of stellar mass possible in early bursts of star-formation (Section 4.4). This is illustrated by the shaded regions in Figure 11. To derive the area in the shaded swaths, we applied the ratio between the mass permitted in early burst at $z_f = 100$ given to the fiducial value (listed in Table 4), interpolated in redshift as above. Therefore, the effects of adding the *MIRI* data both lower SFR (and stellar masses) and limit the total stellar mass allowed in early bursts. The combination of these effects reduces the upper bound on the total cosmic stellar mass density allowed by the data by 0.4 dex at $z = 4$ and by 1.0 dex at $z = 9$. As illustrated in Figure 11, this implies that the *JWST/MIRI* data have constrained the stel-

lar mass in galaxies at $z = 9$ to be less than 0.1% that of the present-day value ($\rho_*(z = 0)$).

5.4. Random Musings

The fact that galaxies are bluer than previous constraints (i.e., they are “bluer than they appear”) has other consequences, and likely dovetails with other recent results from *JWST* NIRC*am* imaging. These results in this *Paper* are likely only the first foray into the properties of distant galaxies using the longer wavelength data available from *MIRI*. Future studies will be able to combine both NIRC*am* and *MIRI* imaging, provide *JWST*-quality data from 0.8 – 10 μm , which will improve the constraints in this *Paper*. Already there are indications using *JWST/NIRCam* data only that the number density of luminous galaxies at $z > 10$ may be much higher than predictions (e.g., Bouwens et al. 2022; Donnan et al. 2022; Finkelstein et al. 2022a; Harikane et al. 2022; Naidu et al. 2022; Robertson et al. 2022). One explanation for these discoveries could be that the UV-luminosity per unit stellar mass (the UV “efficiency”) may be higher than our models predict. This could be a result of changes in the stellar populations (a shift toward bluer/harder ionizing spectra) or a change in the stellar IMF that is weighted toward higher-mass stars.

However, a change in the IMF or in the UV efficiency does not change the conclusion that the light from older stars could be lost in the glare of the more recently formed stars, nor would it change the conclusion that there is less light in general at longer wavelengths from these galaxies. Even if the lower-mass cutoff of the IMF is higher, e.g., $> 50M_\odot$ (Raiter et al. 2010) then after ~ 10 Myr the mass left in such stars would be effectively zero. Therefore, any of these effects would further lower the galaxy M/L values, and therefore lower the stellar masses by even more than what we have measured with the *MIRI* data. (The only way to add more stellar mass in galaxies at this epoch is if there is a substantial population of galaxies at $z > 6$ that are undetected in *HST*, which would be an important discovery for *JWST*). Regardless, the *MIRI* data have better constrained the available light in stars at these early epochs and shown that galaxies contain more than three times less “light” at rest-frame 0.7–1 μm than previously known.

6. CONCLUSIONS

In this *Paper* we have presented results from CEERS on the stellar population parameters for 28 galaxies with redshifts $4 < z < 9$ using new imaging data from *JWST/MIRI* at 5.6 and 7.7 μm . Our galaxy sample was detected in deep data from *HST/WFC3* and ACS and has observations from *Spitzer/IRAC* at 3.6 and 4.5 μm . The *MIRI* 5.6 and 7.7 μm data extend the coverage of the rest-frame spectral energy distribution to nearly 1 micron for galaxies in this redshift range. We use these data to study the improvements in the stellar masses and SFRs of the galaxies at these redshifts when the *MIRI* data are included. Our main results are the following.

- Galaxies at $4 < z < 9$ have bluer rest-frame UV- I -band colors ($m_{1600} - I$). Using the MIRI data we model the SEDs using stellar population synthesis models (with BAGPIPES). When we compare the average galaxy SED (Figure 10) we find that models that include the MIRI data are (on average) $\Delta(m_{1600} - I) \approx 0.4$ mag bluer in their rest-frame colors compared to models that exclude the MIRI data.
- Galaxies generally have lower stellar masses and SFRs when the MIRI data are included. For the majority of the galaxies (Figure 7) adding the MIRI data *reduces* the derived stellar masses by 0.25 dex at $4 < z < 6$ (a factor of 1.8) and by 0.38 dex at $6 < z < 9$ (a factor of 2.4). Similarly including the MIRI data *reduces* the SFRs by 0.15 dex at $4 < z < 6$ (a factor of 1.4) and 0.29 dex at $6 < z < 9$ (a factor of 2).

There are multiple reasons the stellar masses and SFRs are lowered when we include the MIRI data. The first reason is that the galaxies are blue, and the fits favor models with lower dust attenuation and models with lower M/L in general. The second reason is that in many cases the IRAC 3.6 and 4.5 μm data probe the rest-frame optical, and these show indications of containing light from strong emission lines (e.g., redshifted $H\beta + [\text{O III}]$, $H\alpha + [\text{N II}]$, $[\text{O II}]$, etc.). These boost the flux in these bands. In the absence of MIRI data the models can not determine if the red rest-frame UV-optical colors are a result of dust attenuation, older stellar populations, or strong emission lines (or all of them). The parameter constraints then give more weight (probably density) to models with higher stellar masses and SFRs. When the MIRI data are included, then probe more of the stellar continuum at $>7000 \text{ \AA}$ rest-frame. The model fits that include the MIRI data then show the dominant effect in the rest-frame optical are strong nebular emission lines. This problem will persist for models that use NIRCcam data as it also is limited to wavelengths less than 5 μm , but this can be tested with forthcoming datasets.

- The amount of stellar mass that could have formed in early bursts is lower. We estimated the amount of stellar mass formed by using a star-formation history that includes an early burst (at $z_f = 100$) in addition to a smoothly evolving component. A stellar population formed at this early time would fade and redden with time, and it would have the highest M/L at any subsequent time and therefore representations an upper limit on the amount of mass that could exist in these galaxies. The MIRI data improves the constraint on this stellar population by probing longer wavelengths (where the impact from this stellar population is more

pronounced). Figure 9 shows that without the MIRI data, the amount of stellar mass in this population can be as much as 0.9 dex higher at $4 < z < 6$ (a factor of 7) and as much as 1.1 dex higher at $6 < z < 9$ (a factor of >10). Including the MIRI data, these drop to 0.6 dex at $4 < z < 6$ (a factor of 4) and 0.7 dex at $6 < z < 9$ (a factor of 5). Therefore, adding the MIRI reduces the amount of mass in early bursts by a factor of order 2 (compared to when no MIRI data are used).

- Our analysis of the MIRI 5.6 and 7.7 μm therefore provides evidence that there is *less* star-formation in distant galaxies (because the SFRs and stellar masses are lowered) than found in previous studies. The MIRI data also reduce the limits on the amount of stellar mass possibly formed at early times. The combination of these results has implications for the evolution of the cosmic stellar-mass density, ρ_* . We showed (Figure 11) that applying our results to the galaxy population shows that the amount of stellar mass density in galaxies at $z = 9$ is less than 0.1% of the present day, $z = 0$, value. This is an order of magnitude lower than implied by previous studies (i.e., pre-*JWST*).

We wish to thank everyone that brought *JWST* to fruition. We also thank our other colleagues in the CEERS collaboration for their hard work and valuable contributions on this project. CP thanks Marsha and Ralph Schilling for generous support of this research. Portions of this research were conducted with the advanced computing resources provided by Texas A&M High Performance Research Computing (HPRC, <http://hprc.tamu.edu>). This work benefited from support from the George P. and Cynthia Woods Mitchell Institute for Fundamental Physics and Astronomy at Texas A&M University. This work acknowledges support from the NASA/ESA/CSA James Webb Space Telescope through the Space Telescope Science Institute, which is operated by the Association of Universities for Research in Astronomy, Incorporated, under NASA contract NAS5-03127. Support for program No. JWST-ERS01345 was provided through a grant from the STScI under NASA contract NAS5-03127.

Software: AstroPy (Astropy Collaboration et al. 2013), BAGPIPES (Carnall et al. 2018), matplotlib (Hunter 2007), NumPy (van der Walt et al. 2011), *photutils* (Bradley et al. 2020), *PyPHER* (Boucaud et al. 2016a), SE (Bertin & Arnouts 1996), SciPy (Virtanen et al. 2020), Seaborn (Waskom 2021).

Table 5. Observed Properties of the Galaxy Sample

ID	R.A. (J2000) (deg)	Decl. (J2000) (deg)	F160 nJy	E160 (nJy)	F560 (nJy)	E560 (nJy)	F770 (nJy)	E770 (nJy)	z_{phot}	z_{16}	z_{84}	z_{spec}	$\mathcal{P}(z=4)$	$\mathcal{P}(z=5)$	$\mathcal{P}(z=6)$	$\mathcal{P}(z=7)$	$\mathcal{P}(z=8)$	$\mathcal{P}(z=9)$
5090	215.04973	52.89656	102.0	12.5	158.8	17.9	148.0	14.4	4.38	4.18	4.56	-1.000	0.68	0.27	0.00	0.00	0.00	0.00
11329	215.04086	52.90623	49.4	6.9	63.5	20.4	44.5	15.7	4.47	4.15	4.65	-1.000	0.55	0.39	0.00	0.00	0.00	0.00
34813	214.97597	52.920297	82.2	16.2	67.0	16.7	43.9	19.4	4.52	4.17	4.59	-1.000	0.52	0.36	0.00	0.00	0.00	0.00
7600	215.04415	52.898731	564.7	29.4	3283.1	32.4	4101.7	24.8	4.57	4.13	4.65	-1.000	0.62	0.38	0.00	0.00	0.00	0.00
13389	215.03793	52.909329	453.9	29.7	578.3	26.9	661.0	22.0	4.57	4.43	4.61	-1.000	0.38	0.61	0.00	0.00	0.00	0.00
37703	214.99094	52.924279	116.7	11.8	278.9	30.4	61.0	17.5	4.60	4.47	4.70	-1.000	0.22	0.78	0.00	0.00	0.00	0.00
15445	215.02689	52.907215	124.5	14.4	187.8	20.2	116.6	14.9	4.60	4.21	4.84	-1.000	0.24	0.62	0.00	0.00	0.00	0.00
41564	214.98708	52.912734	266.4	13.4	481.6	20.8	276.8	15.7	4.63	4.56	4.71	-1.000	0.03	0.97	0.00	0.00	0.00	0.00
45145	215.00878	52.919869	101.2	15.2	108.6	29.6	69.0	19.3	4.68	4.37	5.20	-1.000	0.15	0.74	0.03	0.00	0.00	0.00
14913	215.02081	52.901523	78.3	14.1	72.8	17.8	9.4	8.9	4.68	4.47	4.94	-1.000	0.19	0.81	0.00	0.00	0.00	0.00
42638	214.97762	52.90349	547.0	31.8	711.4	28.5	596.3	23.4	4.71	4.57	4.77	-1.000	0.02	0.90	0.00	0.00	0.00	0.00
41375	215.00283	52.924312	109.2	15.4	47.2	18.1	119.1	14.8	4.74	4.60	5.13	-1.000	0.07	0.92	0.01	0.00	0.00	0.00
35896	214.98522	52.924266	96.3	10.2	114.5	14.8	110.0	15.3	4.76	4.35	5.33	-1.000	0.06	0.73	0.07	0.00	0.00	0.00
13179	215.04260	52.911968	736.4	23.7	1355.2	26.8	1519.1	21.5	4.78	4.72	4.91	-1.000	0.00	1.00	0.00	0.00	0.00	0.00
19180	215.03170	52.919632	773.3	35.6	749.1	26.0	787.7	19.0	4.93	4.86	4.95	5.077†	0.00	1.00	0.00	0.00	0.00	0.00
37653	214.99190	52.925053	103.1	12.5	154.0	22.2	108.4	18.5	4.95	4.72	5.59	4.899‡	0.06	0.71	0.22	0.00	0.00	0.00
18449	215.02314	52.912683	69.0	10.0	185.0	24.2	165.3	17.6	5.05	4.30	5.57	-1.000	0.14	0.59	0.20	0.00	0.00	0.00
41545	215.00312	52.924103	384.9	18.3	749.2	21.5	656.6	17.5	5.19	5.02	5.44	-1.000	0.00	0.90	0.10	0.00	0.00	0.00
7818	215.02758	52.887744	289.9	21.4	421.4	24.5	399.5	20.9	5.27	4.74	5.46	-1.000	0.02	0.86	0.12	0.00	0.00	0.00
12773	215.03057	52.902606	56.4	12.2	17.0	7.5	71.0	14.1	5.35	4.87	5.43	-1.000	0.00	0.90	0.09	0.00	0.00	0.00
24007	214.95185	52.928275	47.1	4.9	107.8	18.8	56.7	12.6	5.64	5.16	5.79	-1.000	0.00	0.46	0.51	0.00	0.00	0.00
49365	215.00994	52.910669	143.9	14.1	408.5	26.8	541.0	20.6	5.64	5.03	5.82	-1.000	0.01	0.38	0.50	0.00	0.00	0.00
18441	215.03209	52.918972	97.2	11.5	199.6	28.2	169.9	22.0	6.76	5.88	7.24	-1.000	0.00	0.01	0.36	0.48	0.07	0.00
39096	214.98901	52.919652	64.1	8.7	159.5	17.0	57.7	11.2	6.82	6.67	7.08	-1.000	0.00	0.00	0.02	0.97	0.01	0.00
12514	215.03716	52.906712	71.6	13.2	142.3	17.8	50.4	13.6	7.57	6.90	8.41	-1.000	0.00	0.00	0.02	0.39	0.44	0.13
7364	215.03561	52.892208	292.6	17.5	575.7	28.4	611.4	23.1	8.52	7.47	8.68	-1.000	0.00	0.00	0.00	0.17	0.52	0.31
6811	215.03538	52.890666	314.5	13.3	426.8	21.6	404.0	16.9	8.93	8.60	9.05	8.683*	0.00	0.00	0.00	0.00	0.08	0.92
26890	214.96754	52.932966	133.3	8.9	101.9	21.4	60.8	16.8	9.16	8.46	9.24	-1.000	0.00	0.00	0.00	0.00	0.06	0.83

NOTE—References for spectroscopic redshifts: † Stawinski, S., et al., in prep; ‡ WERLS; * Zitrin et al. (2015).

Table 6. Derived Stellar masses, SFRs, and Redshifts including the MIRI [5.6] and [7.7] data.

ID	redshift			$\log M_*/M_\odot$ (dex)			$\log \text{SFR}/M_\odot \text{ yr}^{-1}$ (dex)			“Burst” Mass
	z_{50}	z_{16}	z_{84}	$\log M_{50}$	$\log M_{16}$	$\log M_{84}$	$\log \text{SFR}_{50}$	$\log \text{SFR}_{16}$	$\log \text{SFR}_{84}$	$\log M_*/M_\odot$ (dex)
(1)	(2)	(3)	(4)	(5)	(6)	(7)	(8)	(9)	(10)	(11)
5090	4.33	4.19	4.45	9.01	8.84	9.16	0.59	0.50	0.69	9.55
6811	9.76	9.57	9.88	1.60	1.49	1.72	10.34
7364	8.07	7.35	8.55	9.91	9.72	10.04	1.70	1.57	1.82	10.61
7600	4.41	4.22	4.56	10.54	10.36	10.65	2.09	1.97	2.20	10.93
7818	5.19	4.93	5.39	9.51	9.30	9.64	1.19	1.10	1.29	10.23
11329	4.45	4.31	4.59	8.48	8.14	8.73	0.27	0.17	0.37	9.17
12514	7.69	7.03	8.21	8.78	8.47	9.02	0.70	0.53	0.85	9.45
12773	5.08	4.91	5.24	8.01	7.78	8.24	0.08	-0.18	0.30	8.87
13179	4.79	4.73	4.86	10.07	9.86	10.20	1.71	1.60	1.83	10.57
13389	4.53	4.45	4.60	9.61	9.42	9.75	1.25	1.15	1.37	10.16
14178	4.89	4.76	5.08	8.54	8.29	8.79	0.54	0.35	0.67	9.16
15445	4.59	4.46	4.71	8.92	8.67	9.11	0.63	0.54	0.73	9.36
18441	6.54	5.90	7.11	9.32	9.12	9.46	1.03	0.90	1.17	10.00
18449	4.97	4.43	5.32	9.17	8.93	9.32	0.81	0.67	0.95	9.83
19180	9.72	9.48	9.90	1.54	1.38	1.68	10.14
24007	5.36	5.17	5.52	8.76	8.48	8.91	0.41	0.32	0.53	9.59
26890	8.80	8.61	8.97	8.79	8.46	9.04	0.84	0.50	0.97	9.45
34813	4.38	4.27	4.50	8.26	7.97	8.62	0.33	0.02	0.46	8.97
35896	5.13	4.82	5.40	8.92	8.67	9.08	0.63	0.51	0.76	9.44
37653	8.95	8.58	9.13	0.66	0.53	0.83	9.57
37703	4.63	4.53	4.71	8.41	8.20	8.86	0.47	0.23	0.65	9.21
39096	6.78	6.68	6.87	8.81	8.48	8.98	0.63	0.52	0.75	9.41
41375	4.79	4.66	4.96	8.54	8.27	8.77	0.51	0.34	0.61	9.15
41545	5.13	5.00	5.25	9.80	9.62	9.89	1.38	1.29	1.49	10.32
41564	4.66	4.59	4.74	9.36	9.08	9.52	1.05	0.93	1.17	9.78
42638	4.70	4.64	4.76	9.65	9.39	9.80	1.34	1.20	1.45	10.12
45145	4.72	4.55	4.96	8.59	8.28	8.83	0.51	0.34	0.61	9.52
49365	5.31	5.14	5.52	9.63	9.43	9.75	1.29	1.18	1.42	10.23

NOTE—(1) Galaxy ID; (2)–(4) redshift median (50%-tile), and 16th and 84th-percentiles; galaxies with no redshift use the spectroscopic redshift in Table 5; (5)–(7) stellar mass (50th percentile), and 16th and 84th-percentiles in the delayed- τ model; (8)–(10) SFR median (50th percentile), and 16th and 84th percentiles (all SFRs are averaged over the past 100 Myr) in the delayed- τ model; (11) maximum stellar mass allowed in the “burst” formed at $z_f = 100$, these satisfy the BIC criteria (equation 2 in Section 4.4) and correspond approximately to a 3σ upper limit.

A. IMPACT OF CROWDED SOURCES IN IRAC DATA

One source of potential bias relates to the photometry of our sources in the *Spitzer*/IRAC data. As illustrated in the images (Figure 3) some objects have bright neighbors. In the case of the IRAC images, the light from the wings of these objects can blend with that for our sources. There is a large body of literature on the subject of performing crowded source photometry (Laidler et al. 2007; Labbé et al. 2013; Merlin et al. 2015, 2016). We have used the catalog from (Finkelstein et al. 2022b) who used the *HST*/F160W image as a prior for the locations of sources and neighbors. Source photometry is then carried out using TPHOT (Merlin et al. 2015), which estimates the source flux from objects simultaneously when measuring photometry. While this method is theoretically robust, residuals from poorly modeling ePSFs and changes in galaxy morphology with wavelength (the “Morphological K -correction”, Papovich et al. 2005) can lead to systematic uncertainties in source photometry.

To test if our results are impacted by blended sources in the IRAC bands, we did the following. We first searched around each of the galaxies in our sample and identified galaxies that neighbors in the MIRI 5.6 μm catalog within a radius of $r \leq 3''$ and a magnitude of $[5.6] \leq 26.7$ mag (near the flux limit). We selected neighbors in the MIRI 5.6 μm image as the central wavelength is closest to that of IRAC for our dataset (see Figure 2). The IRAC ePSF has a FWHM of $\approx 2''$, so any source within $3''$ in the MIRI data could therefore have IRAC light blended with our source of interest.

Table 7. Derived Stellar masses, SFRs, and Redshifts excluding the MIRI data.

ID	redshift			$\log M_*/M_\odot$ (dex)			$\log \text{SFR}/M_\odot \text{ yr}^{-1}$ (dex)			“Burst” Mass
	z_{50}	z_{16}	z_{84}	$\log M_{50}$	$\log M_{16}$	$\log M_{84}$	$\log \text{SFR}_{50}$	$\log \text{SFR}_{16}$	$\log \text{SFR}_{84}$	$\log M_*/M_\odot$ (dex)
(1)	(2)	(3)	(4)	(5)	(6)	(7)	(8)	(9)	(10)	(11)
5090	4.32	4.17	4.46	9.08	8.75	9.26	0.61	0.50	0.74	10.00
6811	-1.00	-1.00	-1.00	9.85	9.47	10.12	1.70	1.43	1.98	11.17
7364	8.23	7.42	8.61	9.77	9.48	9.97	1.60	1.38	1.80	10.85
7600	4.42	4.26	4.57	10.53	10.32	10.68	2.10	1.97	2.24	11.17
7818	4.83	4.67	5.17	9.83	9.57	10.02	1.45	1.28	1.61	10.51
11329	4.40	4.24	4.56	8.82	8.50	9.05	0.40	0.24	0.55	9.84
12514	7.38	6.77	8.13	9.30	8.92	9.64	1.10	0.77	1.44	10.41
12773	4.97	4.83	5.15	8.96	8.55	9.22	0.58	0.41	0.78	10.23
13179	4.76	4.71	4.81	10.25	10.03	10.38	1.81	1.70	1.96	10.89
13389	4.52	4.44	4.59	9.82	9.65	9.97	1.37	1.24	1.51	10.41
14178	4.78	4.65	4.92	9.27	8.99	9.45	0.90	0.72	1.07	10.08
15445	4.58	4.45	4.70	9.03	8.70	9.25	0.68	0.55	0.85	10.07
18441	6.61	6.07	6.87	10.18	9.90	10.42	1.94	1.66	2.16	11.11
18449	5.00	4.43	5.41	9.24	8.92	9.47	0.90	0.64	1.10	10.13
19180	-1.00	-1.00	-1.00	10.52	10.31	10.70	2.09	1.90	2.25	11.52
24007	5.28	5.06	5.47	8.93	8.59	9.27	0.58	0.38	0.88	10.40
26890	8.92	8.67	9.17	9.39	9.10	9.67	1.28	1.05	1.51	10.53
34813	4.34	4.23	4.47	8.78	8.40	9.05	0.48	0.39	0.59	9.64
35896	4.88	4.66	5.20	9.23	8.94	9.47	0.93	0.72	1.12	10.08
37653	-1.00	-1.00	-1.00	9.55	9.26	9.75	1.18	1.00	1.36	10.39
37703	4.58	4.48	4.68	9.16	8.90	9.35	0.75	0.62	0.88	9.94
39096	6.73	6.59	6.84	9.04	8.68	9.46	0.80	0.57	1.21	10.03
41375	4.73	4.60	4.87	9.15	8.79	9.34	0.73	0.58	0.91	10.19
41545	5.12	4.98	5.26	9.85	9.61	10.03	1.45	1.31	1.60	10.49
41564	4.64	4.57	4.71	9.56	9.34	9.72	1.15	1.04	1.29	10.18
42638	4.68	4.62	4.75	9.85	9.62	10.01	1.47	1.32	1.64	10.55
45145	4.66	4.52	4.86	9.08	8.71	9.30	0.69	0.53	0.88	9.98
49365	5.43	5.23	5.63	9.45	9.14	9.65	1.09	0.89	1.29	10.31

NOTE—(1) Galaxy ID, (2)–(4) redshift median (50%-tile), and 16th and 84th-percentiles; galaxies with no redshift use the spectroscopic redshift in Table 5; (5)–(7) stellar mass (50th percentile), and 16th and 84th-percentiles in the delayed- τ model; (8)–(10) SFR median (50th percentile), and 16th and 84th percentiles (all SFRs are averaged over the past 100 Myr) in the delayed- τ model; (11) maximum stellar mass allowed in the “burst” formed at $z_f = 100$, these satisfy the BIC criteria (equation 2 in Section 4.4) and correspond approximately to a 3σ upper limit.

From our sample, we identified 11 galaxies that have a neighbor within $3''$ in the MIRI $5.6 \mu\text{m}$ image. To estimate their effect on our study we removed these objects from the sample and recomputed the offsets in stellar mass and SFR for the results that include the MIRI 5.6 and $7.7 \mu\text{m}$ data versus the results that exclude the MIRI data. These results are shown in Figure 12. Contrasting this figure with the one for the full sample (Figure 7) shows there is little change in the median offsets in stellar mass and SFR. The galaxy sample used in this Appendix is obviously smaller, but the median values do not change appreciably. For the sample that excludes blended objects, the offsets in stellar mass are $\Delta \log M_* = 0.21$ dex for $4 < z < 6$ and 0.53 for $6 < z < 9$ (though the later now includes only three galaxies). The offsets in SFR are $\Delta \log \text{SFR} = 0.13$ dex for $4 < z < 6$ and 0.42 dex for $6 < z < 9$. These are within ≈ 0.1 dex of the values reported for the full sample (in Figure 7).

Similarly, we also investigated how the IRAC data for sources with close neighbors impact our finding that the stellar populations of the galaxies in our sample are generally “bluer” when the MIRI data are included in the analysis (see Section 5.1 and Figure 10). We repeated our analysis of the rest-frame colors in Section 5.1 with our sample of galaxies that excludes those objects with a neighboring MIRI $5.6 \mu\text{m}$ source with $[5.6] < 26.7$ mag and within $r \leq 3''$. We find that in this case the relative rest-frame colors change only slightly. The rest-frame far-UV- I color become *bluer* by 0.015 mag (to have a total rest-frame (blue) color of $\Delta(m_{1600} - I) \approx 0.42$ mag) when the objects with crowded IRAC photometry are excluded.

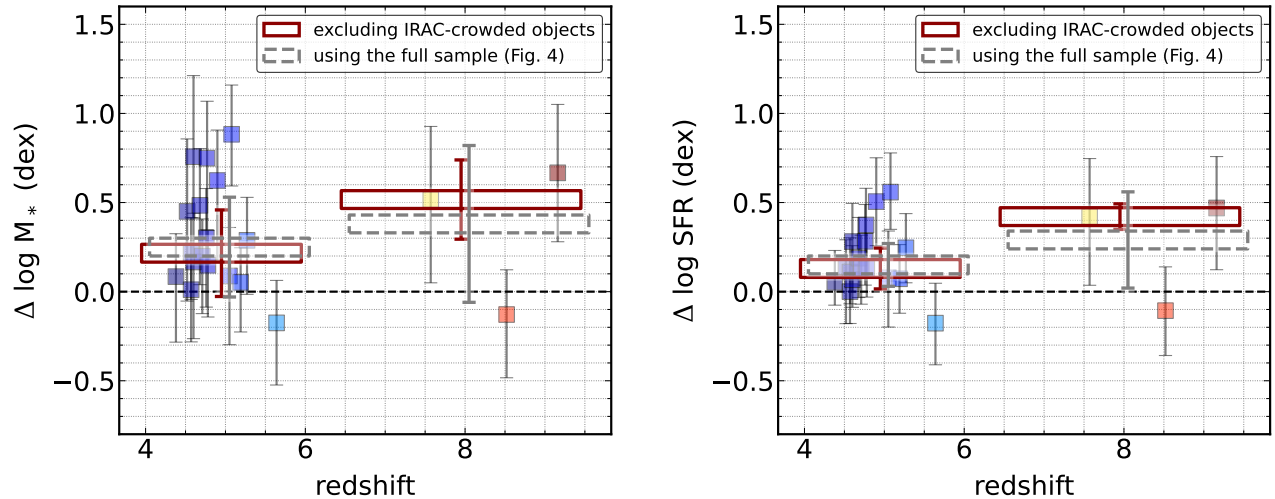


Figure 12. Testing the impact of sources with “crowded” IRAC photometry. The plots in this figure are similar to those in Figure 7, and compare the stellar masses and SFRs derived from the SED modeling for galaxies including the MIRI F560W and F770W data and without the MIRI data. In both panels the results show the difference between the mass (SFR) derived without MIRI data and the mass (SFR) deriving including the MIRI data. In this figure, we have excluded objects that have a neighbor with $r \leq 3''$ and MIRI [5.6] ≤ 26.7 mag. This eliminates 11 objects, and allows us to test if crowding in the IRAC data (which has lower angular resolution) impacts object photometry in the IRAC bands. We do not observe any significant offset compared to the results in Figure 7: the median offsets in stellar mass and SFR change by ≈ 0.1 dex. Therefore we conclude that blended IRAC photometry does not significantly impact the results here.

Therefore, we conclude that our results are not dominated by photometry from sources crowded in the IRAC data. Obviously, future studies using *JWST*/NIRCam will be valuable to testing the IRAC photometry (see, e.g., Bagley et al. 2022).

REFERENCES

- Antwi-Danso, J., Papovich, C., Leja, J., et al. 2022, arXiv e-prints, arXiv:2207.07170. <https://arxiv.org/abs/2207.07170>
- Arellano-Córdova, K. Z., Berg, D. A., Chisholm, J., et al. 2022, ApJL, 940, L23, doi: [10.3847/2041-8213/ac9ab2](https://doi.org/10.3847/2041-8213/ac9ab2)
- Astropy Collaboration, Robitaille, T. P., Tollerud, E. J., et al. 2013, A&A, 558, A33, doi: [10.1051/0004-6361/201322068](https://doi.org/10.1051/0004-6361/201322068)
- Backhaus, B. E., Trump, J. R., Cleri, N. J., et al. 2022, ApJ, 926, 161, doi: [10.3847/1538-4357/ac3919](https://doi.org/10.3847/1538-4357/ac3919)
- Bagley, M. B., Finkelstein, S. L., Koekemoer, A. M., et al. 2022, arXiv e-prints, arXiv:2211.02495. <https://arxiv.org/abs/2211.02495>
- Bailer-Jones, C. A. L. 2017, Practical Bayesian Inference
- Barkana, R., & Loeb, A. 2001, PhR, 349, 125, doi: [10.1016/S0370-1573\(01\)00019-9](https://doi.org/10.1016/S0370-1573(01)00019-9)
- Behroozi, P., & Silk, J. 2018, MNRAS, 477, 5382, doi: [10.1093/mnras/sty945](https://doi.org/10.1093/mnras/sty945)
- Bertin, E., & Arnouts, S. 1996, A&AS, 117, 393
- Bhatawdekar, R., & Conselice, C. J. 2021, ApJ, 909, 144, doi: [10.3847/1538-4357/abdd3f](https://doi.org/10.3847/1538-4357/abdd3f)
- Bisigello, L., Caputi, K. I., Colina, L., et al. 2017, ApJS, 231, 3, doi: [10.3847/1538-4365/aa7a14](https://doi.org/10.3847/1538-4365/aa7a14)
- Boquien, M., Burgarella, D., Roehlly, Y., et al. 2019, A&A, 622, A103, doi: [10.1051/0004-6361/201834156](https://doi.org/10.1051/0004-6361/201834156)
- Boucaud, A., Bocchio, M., Abergel, A., et al. 2016a, PyPHER: Python-based PSF Homogenization kERnels, Astrophysics Source Code Library, record ascl:1609.022. <http://ascl.net/1609.022>
- . 2016b, A&A, 596, A63, doi: [10.1051/0004-6361/201629080](https://doi.org/10.1051/0004-6361/201629080)
- Bouwens, R., Illingworth, G., Oesch, P., et al. 2022, arXiv e-prints, arXiv:2212.06683. <https://arxiv.org/abs/2212.06683>
- Bouwens, R. J., Stefanon, M., Oesch, P. A., et al. 2019, ApJ, 880, 25, doi: [10.3847/1538-4357/ab24c5](https://doi.org/10.3847/1538-4357/ab24c5)
- Bouwens, R. J., Illingworth, G. D., Oesch, P. A., et al. 2012, ApJ, 754, 83, doi: [10.1088/0004-637X/754/2/83](https://doi.org/10.1088/0004-637X/754/2/83)
- Bowman, J. D., Rogers, A. E. E., Monsalve, R. A., Mozdzen, T. J., & Mahesh, N. 2018, Nature, 555, 67, doi: [10.1038/nature25792](https://doi.org/10.1038/nature25792)
- Boylett, K., Mascia, S., Pentericci, L., et al. 2022, arXiv e-prints, arXiv:2207.13459. <https://arxiv.org/abs/2207.13459>

- Boylan-Kolchin, M. 2022, arXiv e-prints, arXiv:2208.01611.
<https://arxiv.org/abs/2208.01611>
- Bradley, L., Sipőcz, B., Robitaille, T., et al. 2020, *astropy/photutils*: 1.0.0, 1.0.0, Zenodo, Zenodo, doi: [10.5281/zenodo.4044744](https://doi.org/10.5281/zenodo.4044744)
- Brinchmann, J. 2022, arXiv e-prints, arXiv:2208.07467.
<https://arxiv.org/abs/2208.07467>
- Bruzual, G., & Charlot, S. 2003, *MNRAS*, 344, 1000,
 doi: [10.1046/j.1365-8711.2003.06897.x](https://doi.org/10.1046/j.1365-8711.2003.06897.x)
- Buat, V., Ciesla, L., Boquien, M., Matek, K., & Burgarella, D. 2019, *A&A*, 632, A79, doi: [10.1051/0004-6361/201936643](https://doi.org/10.1051/0004-6361/201936643)
- Burgarella, D., Theulé, P., Buat, V., et al. 2022, arXiv e-prints, arXiv:2211.05744. <https://arxiv.org/abs/2211.05744>
- Calzetti, D. 2001, *PASP*, 113, 1449, doi: [10.1086/324269](https://doi.org/10.1086/324269)
- Carnall, A. C., Leja, J., Johnson, B. D., et al. 2019, *ApJ*, 873, 44,
 doi: [10.3847/1538-4357/ab04a2](https://doi.org/10.3847/1538-4357/ab04a2)
- Carnall, A. C., McLure, R. J., Dunlop, J. S., & Davé, R. 2018, *MNRAS*, 480, 4379, doi: [10.1093/mnras/sty2169](https://doi.org/10.1093/mnras/sty2169)
- Castellano, M., Pentericci, L., Fontana, A., et al. 2017, *ApJ*, 839, 73, doi: [10.3847/1538-4357/aa696e](https://doi.org/10.3847/1538-4357/aa696e)
- Chabrier, G. 2003, *PASP*, 115, 763, doi: [10.1086/376392](https://doi.org/10.1086/376392)
- Chworowsky, K., Finkelstein, S. L., Spilker, J., et al. 2022, *ApJ*, submitted
- Conroy, C. 2013, *ARA&A*, 51, 393,
 doi: [10.1146/annurev-astro-082812-141017](https://doi.org/10.1146/annurev-astro-082812-141017)
- Curti, M., D'Eugenio, F., Carniani, S., et al. 2023, *MNRAS*, 518, 425, doi: [10.1093/mnras/stac2737](https://doi.org/10.1093/mnras/stac2737)
- Curtis-Lake, E., Carniani, S., Cameron, A., et al. 2022, arXiv e-prints, arXiv:2212.04568. <https://arxiv.org/abs/2212.04568>
- De Barros, S., Oesch, P. A., Labbé, I., et al. 2019, *MNRAS*, 489, 2355, doi: [10.1093/mnras/stz940](https://doi.org/10.1093/mnras/stz940)
- Dickinson, M., Papovich, C., Ferguson, H. C., & Budavári, T. 2003, *ApJ*, 587, 25, doi: [10.1086/368111](https://doi.org/10.1086/368111)
- Diemer, B., Sparre, M., Abramson, L. E., & Torrey, P. 2017, *ApJ*, 839, 26, doi: [10.3847/1538-4357/aa68e5](https://doi.org/10.3847/1538-4357/aa68e5)
- Donnan, C. T., McLeod, D. J., Dunlop, J. S., et al. 2022, *MNRAS*, doi: [10.1093/mnras/stac3472](https://doi.org/10.1093/mnras/stac3472)
- Duncan, K., Conselice, C. J., Mortlock, A., et al. 2014, *MNRAS*, 444, 2960, doi: [10.1093/mnras/stu1622](https://doi.org/10.1093/mnras/stu1622)
- Endsley, R., Stark, D. P., Chevallard, J., & Charlot, S. 2021, *MNRAS*, 500, 5229, doi: [10.1093/mnras/staa3370](https://doi.org/10.1093/mnras/staa3370)
- Endsley, R., Stark, D. P., Whitler, L., et al. 2022, arXiv e-prints, arXiv:2208.14999. <https://arxiv.org/abs/2208.14999>
- Feroz, F., Hobson, M. P., & Bridges, M. 2009, *MNRAS*, 398, 1601, doi: [10.1111/j.1365-2966.2009.14548.x](https://doi.org/10.1111/j.1365-2966.2009.14548.x)
- Finkelstein, S. L. 2016, *PASA*, 33, e037,
 doi: [10.1017/pasa.2016.26](https://doi.org/10.1017/pasa.2016.26)
- Finkelstein, S. L., Papovich, C., Giavalisco, M., et al. 2010, *ApJ*, 719, 1250, doi: [10.1088/0004-637X/719/2/1250](https://doi.org/10.1088/0004-637X/719/2/1250)
- Finkelstein, S. L., Papovich, C., Salmon, B., et al. 2012, *ApJ*, 756, 164, doi: [10.1088/0004-637X/756/2/164](https://doi.org/10.1088/0004-637X/756/2/164)
- Finkelstein, S. L., Bagley, M. B., Arrabal Haro, P., et al. 2022a, arXiv e-prints, arXiv:2207.12474.
<https://arxiv.org/abs/2207.12474>
- Finkelstein, S. L., Bagley, M., Song, M., et al. 2022b, *ApJ*, 928, 52, doi: [10.3847/1538-4357/ac3aed](https://doi.org/10.3847/1538-4357/ac3aed)
- Finkelstein, S. L., Bagley, M. B., Ferguson, H. C., et al. 2022c, arXiv e-prints, arXiv:2211.05792.
<https://arxiv.org/abs/2211.05792>
- Finlator, K., Oppenheimer, B. D., & Davé, R. 2011, *MNRAS*, 410, 1703, doi: [10.1111/j.1365-2966.2010.17554.x](https://doi.org/10.1111/j.1365-2966.2010.17554.x)
- Fujimoto, S., Ouchi, M., Nakajima, K., et al. 2022, arXiv e-prints, arXiv:2212.06863. <https://arxiv.org/abs/2212.06863>
- García-Argumán, Á., Pérez-González, P. G., Gil de Paz, A., et al. 2022, arXiv e-prints, arXiv:2207.14062.
<https://arxiv.org/abs/2207.14062>
- Giménez-Arteaga, C., Oesch, P. A., Brammer, G. B., et al. 2022, arXiv e-prints, arXiv:2212.08670.
<https://arxiv.org/abs/2212.08670>
- Glazebrook, K., Nanayakkara, T., Jacobs, C., et al. 2022, arXiv e-prints, arXiv:2208.03468. <https://arxiv.org/abs/2208.03468>
- Grazian, A., Fontana, A., Santini, P., et al. 2015, *A&A*, 575, A96,
 doi: [10.1051/0004-6361/201424750](https://doi.org/10.1051/0004-6361/201424750)
- Harikane, Y., Ouchi, M., Oguri, M., et al. 2022, arXiv e-prints, arXiv:2208.01612. <https://arxiv.org/abs/2208.01612>
- Heintz, K. E., Giménez-Arteaga, C., Fujimoto, S., et al. 2022, arXiv e-prints, arXiv:2212.06877.
<https://arxiv.org/abs/2212.06877>
- Hunter, J. D. 2007, *Computing in Science and Engineering*, 9, 90,
 doi: [10.1109/MCSE.2007.55](https://doi.org/10.1109/MCSE.2007.55)
- Hutchison, T. A., Papovich, C., Finkelstein, S. L., et al. 2019, *ApJ*, 879, 70, doi: [10.3847/1538-4357/ab22a2](https://doi.org/10.3847/1538-4357/ab22a2)
- Iyer, K. G., Gawiser, E., Faber, S. M., et al. 2019, *ApJ*, 879, 116,
 doi: [10.3847/1538-4357/ab2052](https://doi.org/10.3847/1538-4357/ab2052)
- Kartaltepe, J. S., Rose, C., Vanderhoof, B. N., et al. 2022, arXiv e-prints, arXiv:2210.14713. <https://arxiv.org/abs/2210.14713>
- Katz, H., Saxena, A., Cameron, A. J., et al. 2023, *MNRAS*, 518, 592, doi: [10.1093/mnras/stac2657](https://doi.org/10.1093/mnras/stac2657)
- Kikuchihara, S., Ouchi, M., Ono, Y., et al. 2020, *ApJ*, 893, 60,
 doi: [10.3847/1538-4357/ab7dbe](https://doi.org/10.3847/1538-4357/ab7dbe)
- Koekemoer, A. M., Faber, S. M., Ferguson, H. C., et al. 2011, *ApJS*, 197, 36, doi: [10.1088/0067-0049/197/2/36](https://doi.org/10.1088/0067-0049/197/2/36)
- Kriek, M., van Dokkum, P. G., Labbé, I., et al. 2009, *ApJ*, 700, 221, doi: [10.1088/0004-637X/700/1/221](https://doi.org/10.1088/0004-637X/700/1/221)
- Labbé, I., Oesch, P. A., Bouwens, R. J., et al. 2013, *ApJL*, 777, L19, doi: [10.1088/2041-8205/777/2/L19](https://doi.org/10.1088/2041-8205/777/2/L19)
- Labbé, I., van Dokkum, P., Nelson, E., et al. 2022, arXiv e-prints, arXiv:2207.12446. <https://arxiv.org/abs/2207.12446>
- Laidler, V. G., Papovich, C., Groggin, N. A., et al. 2007, *PASP*, 119, 1325, doi: [10.1086/523898](https://doi.org/10.1086/523898)

- Langeroodi, D., Hjorth, J., Chen, W., et al. 2022, arXiv e-prints, arXiv:2212.02491. <https://arxiv.org/abs/2212.02491>
- Laporte, N., Nakajima, K., Ellis, R. S., et al. 2017, *ApJ*, 851, 40, doi: [10.3847/1538-4357/aa96a8](https://doi.org/10.3847/1538-4357/aa96a8)
- Larson, R. B., & Tinsley, B. M. 1978, *ApJ*, 219, 46, doi: [10.1086/155753](https://doi.org/10.1086/155753)
- Le Fèvre, O., Tasca, L. A. M., Cassata, P., et al. 2015, *A&A*, 576, A79, doi: [10.1051/0004-6361/201423829](https://doi.org/10.1051/0004-6361/201423829)
- Leja, J., Carnall, A. C., Johnson, B. D., Conroy, C., & Speagle, J. S. 2019, *ApJ*, 876, 3, doi: [10.3847/1538-4357/ab133c](https://doi.org/10.3847/1538-4357/ab133c)
- Madau, P., & Dickinson, M. 2014, *ARA&A*, 52, 415, doi: [10.1146/annurev-astro-081811-125615](https://doi.org/10.1146/annurev-astro-081811-125615)
- Matthee, J., Mackenzie, R., Simcoe, R. A., et al. 2022, arXiv e-prints, arXiv:2211.08255. <https://arxiv.org/abs/2211.08255>
- Merlin, E., Fontana, A., Ferguson, H. C., et al. 2015, *A&A*, 582, A15, doi: [10.1051/0004-6361/201526471](https://doi.org/10.1051/0004-6361/201526471)
- Merlin, E., Bourne, N., Castellano, M., et al. 2016, *A&A*, 595, A97, doi: [10.1051/0004-6361/201628751](https://doi.org/10.1051/0004-6361/201628751)
- Miralda-Escudé, J. 2003, *ApJ*, 597, 66, doi: [10.1086/378286](https://doi.org/10.1086/378286)
- Mobasher, B., Dahlen, T., Ferguson, H. C., et al. 2015, *ApJ*, 808, 101, doi: [10.1088/0004-637X/808/1/101](https://doi.org/10.1088/0004-637X/808/1/101)
- Naidu, R. P., Oesch, P. A., van Dokkum, P., et al. 2022, *ApJL*, 940, L14, doi: [10.3847/2041-8213/ac9b22](https://doi.org/10.3847/2041-8213/ac9b22)
- Nanayakkara, T., Glazebrook, K., Jacobs, C., et al. 2022, arXiv e-prints, arXiv:2207.13860. <https://arxiv.org/abs/2207.13860>
- Oesch, P. A., Bouwens, R. J., Illingworth, G. D., et al. 2014, *ApJ*, 786, 108, doi: [10.1088/0004-637X/786/2/108](https://doi.org/10.1088/0004-637X/786/2/108)
- Oesch, P. A., van Dokkum, P. G., Illingworth, G. D., et al. 2015, *ApJL*, 804, L30, doi: [10.1088/2041-8205/804/2/L30](https://doi.org/10.1088/2041-8205/804/2/L30)
- Oke, J. B., & Gunn, J. E. 1983, *ApJ*, 266, 713, doi: [10.1086/160817](https://doi.org/10.1086/160817)
- Papovich, C., Moustakas, L. A., Dickinson, M., et al. 2006, *ApJ*, 640, 92, doi: [10.1086/499915](https://doi.org/10.1086/499915)
- Papovich, C., Dickinson, M., & Ferguson, H. C. 2001, *ApJ*, 559, 620, doi: [10.1086/322412](https://doi.org/10.1086/322412)
- Papovich, C., Dickinson, M., Giavalisco, M., Conselice, C. J., & Ferguson, H. C. 2005, *ApJ*, 631, 101, doi: [10.1086/429120](https://doi.org/10.1086/429120)
- Papovich, C., Finkelstein, S. L., Ferguson, H. C., Lotz, J. M., & Giavalisco, M. 2011, *MNRAS*, 412, 1123, doi: [10.1111/j.1365-2966.2010.17965.x](https://doi.org/10.1111/j.1365-2966.2010.17965.x)
- Papovich, C., Labbé, I., Quadri, R., et al. 2015, *ApJ*, 803, 26, doi: [10.1088/0004-637X/803/1/26](https://doi.org/10.1088/0004-637X/803/1/26)
- Papovich, C., Simons, R. C., Estrada-Carpenter, V., et al. 2022, *ApJ*, 937, 22, doi: [10.3847/1538-4357/ac8058](https://doi.org/10.3847/1538-4357/ac8058)
- Pérez-González, P. G., Rieke, G. H., Villar, V., et al. 2008, *ApJ*, 675, 234, doi: [10.1086/523690](https://doi.org/10.1086/523690)
- Pérez-González, P. G., Barro, G., Annunziatella, M., et al. 2022, arXiv e-prints, arXiv:2211.00045. <https://arxiv.org/abs/2211.00045>
- Pfarr, J., Maraston, C., & Tonini, C. 2012, *MNRAS*, 422, 3285, doi: [10.1111/j.1365-2966.2012.20848.x](https://doi.org/10.1111/j.1365-2966.2012.20848.x)
- Planck Collaboration, Aghanim, N., Akrami, Y., et al. 2020, *A&A*, 641, A6, doi: [10.1051/0004-6361/201833910](https://doi.org/10.1051/0004-6361/201833910)
- Raiter, A., Schaerer, D., & Fosbury, R. A. E. 2010, *A&A*, 523, A64, doi: [10.1051/0004-6361/201015236](https://doi.org/10.1051/0004-6361/201015236)
- Rigby, J., Perrin, M., McElwain, M., et al. 2022, arXiv e-prints, arXiv:2207.05632. <https://arxiv.org/abs/2207.05632>
- Roberts-Borsani, G. W., Ellis, R. S., & Laporte, N. 2020, *MNRAS*, 497, 3440, doi: [10.1093/mnras/staa2085](https://doi.org/10.1093/mnras/staa2085)
- Roberts-Borsani, G. W., Bouwens, R. J., Oesch, P. A., et al. 2016, *ApJ*, 823, 143, doi: [10.3847/0004-637X/823/2/143](https://doi.org/10.3847/0004-637X/823/2/143)
- Robertson, B. E., Tacchella, S., Johnson, B. D., et al. 2022, arXiv e-prints, arXiv:2212.04480. <https://arxiv.org/abs/2212.04480>
- Sanders, R. L., Shapley, A. E., Kriek, M., et al. 2016, *ApJ*, 816, 23, doi: [10.3847/0004-637X/816/1/23](https://doi.org/10.3847/0004-637X/816/1/23)
- Sanders, R. L., Shapley, A. E., Reddy, N. A., et al. 2020, *MNRAS*, 491, 1427, doi: [10.1093/mnras/stz3032](https://doi.org/10.1093/mnras/stz3032)
- Santini, P., Castellano, M., Fontana, A., et al. 2022a, *ApJ*, 940, 135, doi: [10.3847/1538-4357/ac9a48](https://doi.org/10.3847/1538-4357/ac9a48)
- Santini, P., Fontana, A., Castellano, M., et al. 2022b, arXiv e-prints, arXiv:2207.11379. <https://arxiv.org/abs/2207.11379>
- Schaerer, D., Marques-Chaves, R., Barrufet, L., et al. 2022, arXiv e-prints, arXiv:2207.10034. <https://arxiv.org/abs/2207.10034>
- Skelton, R. E., Whitaker, K. E., Momcheva, I. G., et al. 2014, *ApJS*, 214, 24, doi: [10.1088/0067-0049/214/2/24](https://doi.org/10.1088/0067-0049/214/2/24)
- Smit, R., Bouwens, R. J., Labbé, I., et al. 2014, *ApJ*, 784, 58, doi: [10.1088/0004-637X/784/1/58](https://doi.org/10.1088/0004-637X/784/1/58)
- Smit, R., Bouwens, R. J., Franx, M., et al. 2015, *ApJ*, 801, 122, doi: [10.1088/0004-637X/801/2/122](https://doi.org/10.1088/0004-637X/801/2/122)
- Song, M., Finkelstein, S. L., Ashby, M. L. N., et al. 2016, *ApJ*, 825, 5, doi: [10.3847/0004-637X/825/1/5](https://doi.org/10.3847/0004-637X/825/1/5)
- Stark, D. P., Richard, J., Charlot, S., et al. 2015, *MNRAS*, 450, 1846, doi: [10.1093/mnras/stv688](https://doi.org/10.1093/mnras/stv688)
- Stark, D. P., Ellis, R. S., Charlot, S., et al. 2017, *MNRAS*, 464, 469, doi: [10.1093/mnras/stw2233](https://doi.org/10.1093/mnras/stw2233)
- Stefanon, M., Bouwens, R. J., Illingworth, G. D., et al. 2022, *ApJ*, 935, 94, doi: [10.3847/1538-4357/ac7e44](https://doi.org/10.3847/1538-4357/ac7e44)
- Stefanon, M., Bouwens, R. J., Labbé, I., et al. 2021, *ApJ*, 922, 29, doi: [10.3847/1538-4357/ac1bb6](https://doi.org/10.3847/1538-4357/ac1bb6)
- Stefanon, M., Yan, H., Mobasher, B., et al. 2017, *ApJS*, 229, 32, doi: [10.3847/1538-4365/aa66cb](https://doi.org/10.3847/1538-4365/aa66cb)
- Steinhardt, C. L., Kokorev, V., Rusakov, V., Garcia, E., & Sneppen, A. 2022, arXiv e-prints, arXiv:2208.07879. <https://arxiv.org/abs/2208.07879>
- Sun, F., Egami, E., Pirzkal, N., et al. 2022, arXiv e-prints, arXiv:2209.03374. <https://arxiv.org/abs/2209.03374>
- Tang, M., Stark, D. P., Chevallard, J., & Charlot, S. 2019, *MNRAS*, 489, 2572, doi: [10.1093/mnras/stz2236](https://doi.org/10.1093/mnras/stz2236)
- Tinsley, B. M. 1980, *FCPh*, 5, 287, doi: [10.48550/arXiv.2203.02041](https://doi.org/10.48550/arXiv.2203.02041)

- Topping, M. W., Stark, D. P., Endsley, R., et al. 2022, arXiv e-prints, arXiv:2208.01610. <https://arxiv.org/abs/2208.01610>
- Tran, K.-V. H., Forrest, B., Alcorn, L. Y., et al. 2020, ApJ, 898, 45, doi: [10.3847/1538-4357/ab8cba](https://doi.org/10.3847/1538-4357/ab8cba)
- Trump, J. R., Arrabal Haro, P., Simons, R. C., et al. 2022, arXiv e-prints, arXiv:2207.12388. <https://arxiv.org/abs/2207.12388>
- van der Walt, S., Colbert, S. C., & Varoquaux, G. 2011, Computing in Science and Engineering, 13, 22, doi: [10.1109/MCSE.2011.37](https://doi.org/10.1109/MCSE.2011.37)
- van der Wel, A., Straughn, A. N., Rix, H. W., et al. 2011, ApJ, 742, 111, doi: [10.1088/0004-637X/742/2/111](https://doi.org/10.1088/0004-637X/742/2/111)
- Virtanen, P., Gommers, R., Oliphant, T. E., et al. 2020, Nature Methods, 17, 261, doi: [10.1038/s41592-019-0686-2](https://doi.org/10.1038/s41592-019-0686-2)
- Visbal, E., Bryan, G. L., & Haiman, Z. 2020, ApJ, 897, 95, doi: [10.3847/1538-4357/ab994e](https://doi.org/10.3847/1538-4357/ab994e)
- Wagner, A. Y., Bicknell, G. V., Umemura, M., Sutherland, R. S., & Silk, J. 2016, Astronomische Nachrichten, 337, 167, doi: [10.1002/asna.201512287](https://doi.org/10.1002/asna.201512287)
- Waskom, M. L. 2021, Journal of Open Source Software, 6, 3021, doi: [10.21105/joss.03021](https://doi.org/10.21105/joss.03021)
- Whitler, L., Endsley, R., Stark, D. P., et al. 2022, MNRAS, doi: [10.1093/mnras/stac3535](https://doi.org/10.1093/mnras/stac3535)
- Wilkins, S. M., Bouwens, R. J., Oesch, P. A., et al. 2016, MNRAS, 455, 659, doi: [10.1093/mnras/stv2263](https://doi.org/10.1093/mnras/stv2263)
- Wise, J. H., Turk, M. J., Norman, M. L., & Abel, T. 2012, ApJ, 745, 50, doi: [10.1088/0004-637X/745/1/50](https://doi.org/10.1088/0004-637X/745/1/50)
- Yang, G., Papovich, C., & CEERS Collaboration. 2022 in prep, in prep
- Yoshida, N., Abel, T., Hernquist, L., & Sugiyama, N. 2003, ApJ, 592, 645, doi: [10.1086/375810](https://doi.org/10.1086/375810)
- Zitrin, A., Labbé, I., Belli, S., et al. 2015, ApJL, 810, L12, doi: [10.1088/2041-8205/810/1/L12](https://doi.org/10.1088/2041-8205/810/1/L12)